

# Production of N<sub>2</sub> Vegard-Kaplan and other triplet band emissions in the dayglow of Titan

Anil Bhardwaj\*, Sonal Kumar Jain

Space Physics Laboratory, Vikram Sarabhai Space Centre, Trivandrum 695022, India

## Abstract

Recently the Cassini Ultraviolet Imaging Spectrograph (UVIS) has revealed the presence of N<sub>2</sub> Vegard-Kaplan (VK) band ( $A^3\Sigma_u^+ - X^1\Sigma_g^+$ ) emissions in Titan's dayglow limb observation. We present model calculations for the production of various N<sub>2</sub> triplet states (viz.,  $A^3\Sigma_u^+$ ,  $B^3\Pi_g$ ,  $C^3\Pi_u$ ,  $E^3\Sigma_u$ ,  $W^3\Delta_u$ , and  $B'^3\Sigma_u^+$ ) in the upper atmosphere of Titan. The Analytical Yield Spectra technique is used to calculate steady state photoelectron fluxes in Titan's atmosphere, which are in agreement with those observed by the Cassini's CAPS instrument. Considering direct electron impact excitation, inter-state cascading, and quenching effects, the population of different levels of N<sub>2</sub> triplet states are calculated under statistical equilibrium. Densities of all vibrational levels of each triplet state and volume production rates for various triplet states are calculated in the model. Vertically integrated overhead intensities for the same date and lighting conditions as the reported by UVIS observations for N<sub>2</sub> Vegard-Kaplan ( $A^3\Sigma_u^+ - X^1\Sigma_g^+$ ), First Positive ( $B^3\Pi_g - A^3\Sigma_u^+$ ), Second Positive ( $C^3\Pi_u - B^3\Pi_g$ ), Wu-Benesch ( $W^3\Delta_u - B^3\Pi_g$ ), and Reverse First Positive bands of N<sub>2</sub> are found to be 132, 114, 19, 22, and 22 R, respectively. Overhead intensities are calculated for each vibrational transition of all the triplet band emissions of N<sub>2</sub>, which span a wider spectrum of wavelengths from ultraviolet to infrared. The calculated limb intensities of total and prominent transitions of VK band are presented. The model limb intensity of VK emission within the 150–190 nm wavelength region is in good agreement with the Cassini UVIS observed limb profile. An assessment of the impact of solar EUV flux on the N<sub>2</sub> triplet band emission intensity has been made by using three different solar flux models, viz., Solar EUV Experiment (SEE), SOLAR2000 (S2K) model of Tobiska (2004), and HEUVAC model of Richards et al. (2006). The calculated N<sub>2</sub> VK band intensity at the peak of limb intensity due to S2K and HEUVAC solar flux models is a factor of 1.2 and 0.9, respectively, of that obtained using SEE solar EUV flux. The effects of higher N<sub>2</sub> density and solar zenith angle on the emission intensity are also studied. The model predicted N<sub>2</sub> triplet band intensities during moderate (F10.7 = 150) and high (F10.7 = 240) solar activity conditions, using SEE solar EUV flux, are a factor of 2 and 2.8, respectively, higher than those during solar minimum (F10.7 = 68) condition.

**Keywords:** Titan, Titan Atmosphere, Ultraviolet observations, Upper atmosphere, Aeronomy, N<sub>2</sub> emission, Dayglow

## 1. Introduction

The Saturnian satellite Titan, the second biggest satellite in the solar system, is in many ways the closest analogue to Earth. Like Earth, Titan's atmosphere is dominated by N<sub>2</sub>. Hence, it is natural to expect that Titan's airglow will be dominated by emissions of N<sub>2</sub> and its dissociation product N. In addition to N<sub>2</sub>, Titan

also contains a few percent CH<sub>4</sub> in its atmosphere, with a mixing ratio of about 3% near 1000 km altitude (De La Haye et al., 2007; Strobel et al., 2009).

The Voyager 1 Ultraviolet Spectrometer (UVS) provided the first ultraviolet (UV) airglow observation of Titan in the 53–170 nm band (Broadfoot et al., 1981). The extreme ultraviolet spectrum was dominated by emissions near 95–99 nm, which were attributed to N<sub>2</sub> Carroll-Yoshino (CY)  $c_4'^1\Sigma_u^+ - X^1\Sigma_g^+$  (0, 0) and (0, 1) Rydberg bands (Strobel and Shemansky, 1982). Far ultraviolet emissions present were LBH bands of N<sub>2</sub>, and N and N<sup>+</sup> lines (Broadfoot et al., 1981; Strobel and Shemansky, 1982). By employing multiple scattering

\*Corresponding author. Fax: +91 471 2706535

Email addresses: anil\_bhardwaj@vssc.gov.in;  
bhardwaj\_spl@yahoo.com (Anil Bhardwaj),  
sonaljain.spl@gmail.com (Sonal Kumar Jain)

model for CY band emissions, Stevens (2001) showed that CY (0–0) should be weak and undetectable, while CY (0–1) should be prominent emission at 981 nm and the features at 950 nm are N I lines. Thus, there is no need to invoke magnetospheric electron impact excitation (Stevens, 2001).

After Voyager UVS, Cassini Ultraviolet Imaging Spectrograph (UVIS) provided the next observation of Titan’s airglow in the extreme ultraviolet (EUV, 56.1–118.2 nm) and far ultraviolet (FUV, 115.5–191.3 nm) wavelengths (Ajello et al., 2007, 2008). These disk observations of Titan on 13 Dec. 2004 showed the presence of N<sub>2</sub> LBH bands, atomic multiplets of NI and N<sup>+</sup> lines, and features at 156.1 and 165.7 nm reportedly from CI (Ajello et al., 2008). Recently, limb observation of Titan by UVIS obtained on 22 June 2009 has revealed the presence of N<sub>2</sub> Vegard-Kaplan (VK) ( $A^3\Sigma_u^+ - X^1\Sigma_g^+$ ) bands in the FUV spectrum (Stevens et al., 2011). Also, no CI emissions are reported to be observed. Stevens et al. (2011) showed that model emissions in the 150–190 nm VK band are consistent with UVIS observations.

The N<sub>2</sub> VK bands are a common feature in N<sub>2</sub> atmospheres and have been studied extensively on Earth (e.g., Cartwright, 1978; Meier, 1991; Broadfoot et al., 1997). The N<sub>2</sub> VK bands have been observed recently on Mars by SPICAM aboard Mars Express (Leblanc et al., 2006, 2007; Jain and Bhardwaj, 2011). These emission can also be observed on Venus by SPICAV on-board Venus Express (Bhardwaj and Jain, 2011), but the bright sunlit limb causes a problem in resolving the dayglow emission from scattered light from clouds.

This paper presents a detailed model calculation for the production of N<sub>2</sub> triplet band emissions on Titan, including the recently observed N<sub>2</sub> VK bands. The model includes interstate cascading and quenching, and uses the Analytical Yield Spectra approach for the calculation of electron impact excitation of triplet bands, and is similar to the model used for studying the N<sub>2</sub> triplet emissions on Mars (Jain and Bhardwaj, 2011) and Venus (Bhardwaj and Jain, 2011). We also present the overhead emission intensities of triplet bands, which lie in ultraviolet, visible, and infrared wavelengths. The calculated limb profile of N<sub>2</sub> VK 150–190 nm emission is compared with the Cassini UVIS observation. Impact on the intensity of N<sub>2</sub> triplet emissions due to changes in the solar EUV flux model, solar activity, and Titan’s N<sub>2</sub> density are discussed.

The N<sub>2</sub> triplet band emissions span a wide spectrum of electromagnetic radiation covering EUV-FUV-MUV, visible, and infrared (Jain and Bhardwaj, 2011; Bhardwaj and Jain, 2011). Major emissions in N<sub>2</sub> VK band lie

in the wavelength range 200–400 nm, and a few significant emissions in the visible. N<sub>2</sub> triplet First Positive ( $B \rightarrow A$ ), Wu-Benesch ( $W \rightarrow B$ ), and  $B' \rightarrow B$  bands have prominent emissions in the infrared region. Thus, beside observations of Titan’s dayglow by the Cassini UVIS in EUV and FUV region, the Cassini Visual and Infrared Mapping Spectrometer (VIMS), which has a wide spectral range 300–5100 nm (Brown et al., 2004) and Imaging Science Subsystem (ISS, 250–1100 nm) (Porco et al., 2004), might be able to detect some of the bright emissions of N<sub>2</sub> triplet bands in the MUV, visible, and infrared wavelengths predicted by our model. The model calculations presented in the paper would also be useful for any N<sub>2</sub>-containing planetary atmospheres.

## 2. Model Input

The N<sub>2</sub> density profile in our model is based on the observation made by Huygens Atmospheric Structure Instrument (HASI) on-board Huygens probe (Fulchignoni et al., 2005). Following the approach of Stevens et al. (2011), the density of N<sub>2</sub> is reduced by a factor of 3.1 to bring the HASI N<sub>2</sub> density at 950 km to the level of measured density by Ion and Neutral Mass Spectrometer (INMS) (De La Haye et al., 2007) aboard the Cassini spacecraft. Since reduction in N<sub>2</sub> density affects the altitude of peak production of N<sub>2</sub> triplet bands, the effect of higher N<sub>2</sub> density on emission intensities is discussed in the Section 4.3. Density of CH<sub>4</sub> in our model is based on the UVIS stellar occultation experiment reported by Shemansky et al. (2005).

Photoabsorption and photoionization cross sections of N<sub>2</sub> and CH<sub>4</sub> are taken from photo-cross sections and rate coefficients database (<http://amop.space.swri.edu>) (Huebner et al., 1992). The branching ratios for excited states of N<sub>2</sub><sup>+</sup> and CH<sub>4</sub><sup>+</sup> are taken from Avakyan et al. (1998). Franck-Condon factors and transition probabilities required for calculating the intensity of a specific band  $\nu' - \nu''$  of N<sub>2</sub> are taken from Gilmore et al. (1992). Inelastic cross sections for the electron impact on N<sub>2</sub> are taken from Jackman et al. (1977), except for the triplet states, which are taken from Itikawa (2006), and fitted analytically for ease of usage in the model (Jackman et al., 1977; Bhardwaj and Jain, 2009, 2011; Jain and Bhardwaj, 2011). The fitted parameters are given in Jain and Bhardwaj (2011).

The solar EUV flux is a crucial input required in modelling the upper atmospheric dayglow emissions. The solar EUV flux directly controls the photoelectron production rate, and hence the intensity of emission in the planetary atmosphere that is produced by electron impact excitation, like N<sub>2</sub> triplet band emissions, since

all transitions between the triplet states of  $N_2$  and the ground state are spin forbidden. We have used the solar irradiance measured at Earth (between 2.5 to 120.5 nm) by Solar EUV Experiment (SEE, Version 10.2) (Woods et al., 2005; Lean et al., 2011) on 23 June 2009 (F10.7 = 68) at 1 nm spectral resolution. The solar flux has been scaled to the Sun-Titan distance (9.57 AU) to account for the weaker flux on Titan. To evaluate the impact of solar EUV flux model on emission intensities we have also used solar EUV flux from SOLAR2000 (S2K) v.2.36 model of Tobiska (2004) and HEUVAC solar EUV flux model of Richards et al. (2006) for the same day. All calculations are made at solar zenith angle of  $60^\circ$  unless otherwise mentioned in the text.

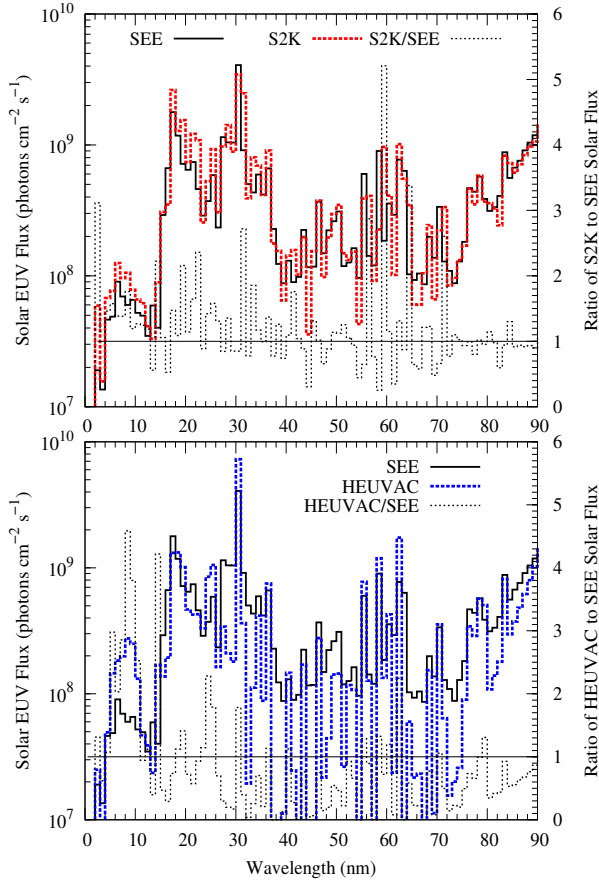


Figure 1: Comparison of SEE, S2K, and HEUVAC solar EUV flux models on 23 June 2009 at 1 AU. (top) SEE solar EUV flux compared with S2K. (bottom) SEE solar EUV flux comparison with HEUVAC. The ratio of solar EUV fluxes is also shown with magnitude on right side Y-axis. Thin solid horizontal line depicts the S2K/SEE and HEUVAC/SEE solar flux ratio = 1.

Figure 1 (top panel) shows the solar EUV fluxes at 1 AU generated using SEE and S2K model on 23 June

2009. Ratio of S2K and SEE solar EUV flux is also shown in the figure. Above 60 nm the SEE and S2K model solar EUV fluxes are in general agreement with each other, but below 60 nm the solar flux of S2K model is higher than that from SEE model. Higher EUV flux at shorter wavelengths would result in larger number of higher energy photoelectrons; hence, volume production rates calculated using S2K solar EUV flux is expected to be higher than that obtained using SEE solar EUV flux (see Section 4.1).

Figure 1 (bottom panel) shows the comparison of SEE solar EUV flux with the solar flux calculated using HEUVAC model, with both the daily F10.7 and the F10.7–81 days average values set to 68 (in units of  $10^{-22} W m^{-2} Hz^{-1}$ ), conditions appropriate for the date of the UVIS limb observations reported by Stevens et al. (2011). Since the HEUVAC model provides solar flux up to 105 nm only, the flux in the 105–120.5 nm range is assumed the same as that in the SEE model. Since the solar flux at higher ( $> 105$  nm) wavelengths does not contribute to the photoelectron production, the inclusion of SEE solar flux in the HEUVAC model at wavelengths higher than 105 nm would not affect our calculation results. At wavelength above 30 nm HEUVAC solar fluxes are smaller than those of SEE model, but at shorter ( $< 30$  nm) wavelengths HEUVAC fluxes are higher than SEE model fluxes. At a few shorter ( $< 15$  nm) wavelengths HEUVAC solar fluxes are as high as a factor of 4 compared to SEE solar flux. The photoelectrons produced due to larger solar fluxes at shorter wavelengths in HEUVAC model would result in larger number of higher energy photoelectrons that can go deeper in the atmosphere, hence a significant lowering of the peak of volume production rate is expected when the HEUVAC solar EUV flux is used (see following section).

### 3. Results and discussion

#### 3.1. Photoelectron Flux

To calculate the photoelectron flux we have adopted the Analytical Yield Spectra (AYS) technique (cf. Singhal and Haider, 1984; Bhardwaj and Singhal, 1990; Bhardwaj et al., 1990, 1996; Singhal and Bhardwaj, 1991; Bhardwaj, 1999, 2003; Bhardwaj and Michael, 1999a,b). The AYS is the analytical representation of numerical yield spectra obtained using the Monte Carlo model (cf. Singhal et al., 1980; Singhal and Bhardwaj, 1991; Bhardwaj and Michael, 1999a,b; Bhardwaj and Jain, 2009). Using AYS the photoelectron flux has been

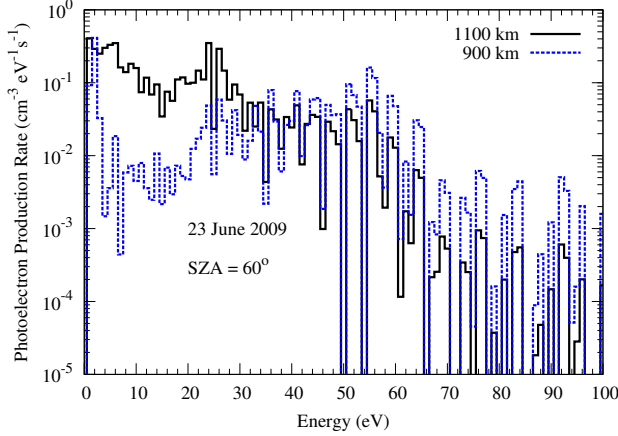


Figure 2: Calculated photoelectron production spectrum at 1100 and 900 km at SZA = 60° using SEE solar EUV flux on 23 June 2009.

calculated as (e.g., Singhal and Haider, 1984; Bhardwaj and Michael, 1999b)

$$\phi(Z, E) = \int_{W_{kl}}^{100} \frac{Q(Z, E)U(E, E_0)}{\sum_l n_l(Z)\sigma_{IT}(E)} dE_0 \quad (1)$$

where  $\sigma_{IT}(E)$  is the total inelastic cross section for the  $l$ th gas, at energy  $E$ ,  $n_l(Z)$  is its density at altitude  $Z$ ,  $W_{kl}$  is the threshold of  $k$ th excited state of gas  $l$ , and  $U(E, E_0)$  is the two-dimensional AYS, which embodies the non-spatial information of electron degradation process. It represents the equilibrium number of electrons per unit energy at an energy  $E$  resulting from the local energy degradation of an incident electron of energy  $E_0$ . For the  $N_2$  gas it is given as (Singhal et al., 1980)

$$U(E, E_0) = C_0 + C_1(E_k + K)/[(E - M)^2 + L^2]. \quad (2)$$

Here  $C_0$ ,  $C_1$ ,  $K$ ,  $M$ , and  $L$  are the fitted parameters which are independent of the energy, and whose values are given by Singhal et al. (1980). The term  $Q(Z, E)$  in equation (1) is the primary photoelectron production rate (cf. Bhardwaj and Singhal, 1990; Michael and Bhardwaj, 1997; Bhardwaj, 2003; Jain and Bhardwaj, 2011). Figure 2 shows the calculated energy spectrum for photoelectron production at 900 and 1100 km on 23 June 2009 at SZA=60° using SEE solar EUV flux. Prominent peaks around 24–26 eV are due to the ionization of  $N_2$  in different excited states by the solar He II Lyman- $\alpha$  line at 303.78 Å. Photoelectron energy spectrum below 25 eV at altitude of 900 km is smaller than that at 1100 km, since electrons below 25 eV mainly produced by solar EUV photons > 30 nm which are attenuated at higher altitudes (> 900 km). Higher energy

photons can still penetrate deeper in the atmosphere and attain unit optical depth at lower altitudes (< 1100 km). That is why photoelectron production spectrum at higher energies (> 50 eV) is higher at 900 km compared to electron spectrum at 1100 km.

During the degradation of photoelectrons in the atmosphere of Titan we have not considered  $CH_4$  since  $N_2$  is the dominant species. Contribution of  $CH_4$ , which is having a mixing ratio of ~3% near 1000 km, to the photoelectron flux is less than 10% (Stevens et al., 2011). The effect of omitting the  $CH_4$  contribution in the photoelectron production rate is less than 5% in our calculation. Stevens et al. (2011) also have stated that neglecting the  $CH_4$  contribution in the calculation of photoelectron production rate results in only less than 5% enhancement in the EUV and FUV volume production rates for the UVIS observation conditions.

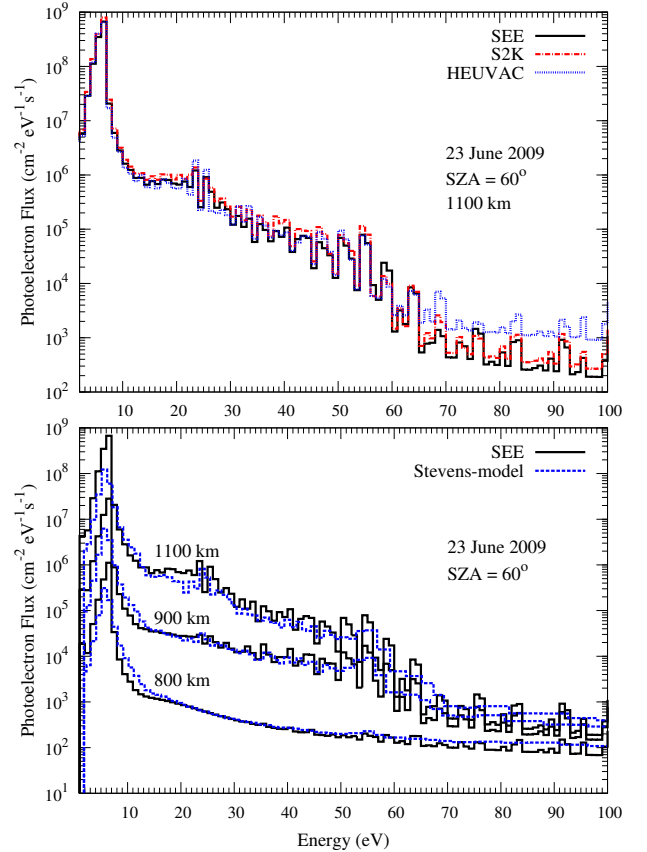


Figure 3: (top panel) Model calculated photoelectron flux at 1100 km using SEE, SOLAR2000 (S2K), and HEUVAC solar flux models. (bottom panel) Comparison of model calculated photoelectron fluxes using SEE solar EUV flux at 800, 900, and 1100 km with those of Stevens et al. (2011).

Figure 3 (top panel) shows the steady state photoelectron flux at altitude of 1100 km and solar zenith angle  $60^\circ$ . Around 6 eV, photoelectron flux is maximum with a value of few  $10^8 \text{ cm}^{-2} \text{ s}^{-1} \text{ eV}^{-1}$ . Due to the degradation of electrons in the atmosphere, the photoelectron flux is smoother compared to the photoelectron production energy spectrum (cf. Fig. 2); still prominent peak can be seen in the flux, *e.g.*, peak at 24 eV is present in the photoelectron flux. Photoelectron fluxes calculated by using S2K and HEUVAC solar EUV fluxes are also shown in Figure 3. As discussed in Section 2, due to higher solar EUV flux in the S2K model, the photoionization yield is slightly higher compared to that in the SEE model, which is responsible for the higher photoelectron flux when S2K model is used. Whereas at energies below 60 eV, photoelectron flux calculated using HEUVAC model is lower than that calculated using SEE solar EUV flux, but at higher energies ( $>60 \text{ eV}$ ) photoelectron flux calculated using HEUVAC model is higher than that calculated using both SEE and S2K models. Higher photoelectron flux at higher energies ( $>60 \text{ eV}$ ) for HEUVAC model is due to the higher solar EUV flux at shorter wavelengths (cf. Figure 1).

Figure 3 (bottom panel) shows the steady state photoelectron fluxes at three different altitudes along with the calculated photoelectron fluxes of Stevens et al. (2011). At and below 6 eV, our calculated photoelectron flux is higher than that of Stevens et al. (2011). This is due to the lack of electron-electron collision loss consideration in our model, which is an important electron energy loss process below 10 eV (Bhardwaj et al., 1990; Bhardwaj and Raghuram, 2011). Between 6 and 15 eV, calculated photoelectron fluxes of Stevens et al. (2011) are higher than our calculated values at all altitudes. At 1100 km, our calculated photoelectron flux between 15 and 25 eV is higher than that of Stevens et al. (2011). This difference in the photoelectron flux between two model calculations may be due to the slightly different treatment of the altitude dependence of electron degradation in both models. In our model, the AYS approach used for the calculation of photoelectron flux is based on the Monte Carlo model (cf. Singhal et al., 1980; Singhal and Bhardwaj, 1991; Bhardwaj and Singhal, 1993; Bhardwaj and Michael, 1999a,b; Bhardwaj and Jain, 2009), while in the AURIC model (Strickland et al., 1999) it is based on the solution of Boltzmann equation. Above 25 eV, the photoelectron flux calculated by Stevens et al. (2011) is consistent with our model values. The peak structures in our calculated photoelectron flux are slightly different than the photoelectron flux of Stevens et al. (2011). This difference is due to the different branching ratios used in both models. In our model,

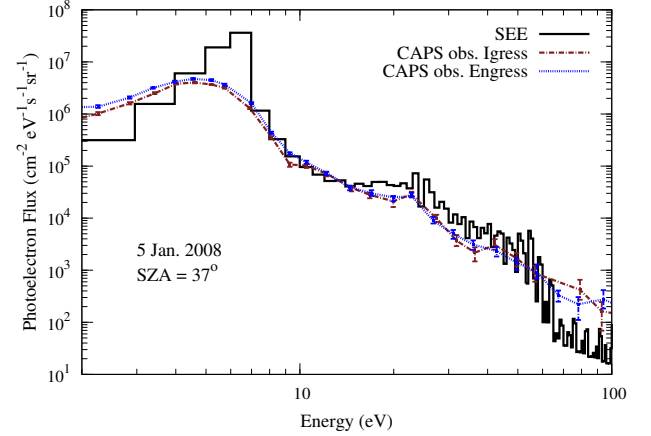


Figure 4: Model calculated photoelectron flux on 5 Jan. 2008 at altitude of 1100 km obtained by using SEE solar EUV flux compared with the Cassini CAPS observation taken from Lavvas et al. (2011).

stable branching ratios taken from Avakyan et al. (1998) are used, whereas in AURIC model branching ratios are wavelength dependent.

To compare the calculated photoelectron flux with Cassini observations we have run our model taking the HASI  $\text{N}_2$  density and SEE solar EUV flux on 5 January 2008 ( $F_{10.7} = 79.7$ ) at  $\text{SZA} = 37^\circ$ . Figure 4 shows the model calculated photoelectron flux at 1100 km along with the photoelectron flux observed by the CAPS instrument (energy resolution  $\Delta E/E = 16.7\%$ ) on-board Cassini taken from Lavvas et al. (2011). Model calculated photoelectron flux agrees well with the observed flux between 7 and  $\sim 20 \text{ eV}$ . Above 20 eV model predicted photoelectron flux is slightly higher than the observation. At higher energies ( $>60 \text{ eV}$ ) the calculated photoelectron flux starts decreasing sharply compared to the observed flux. Lavvas et al. have also observed similar differences in their calculated and the observed photoelectron flux at energies  $> 60 \text{ eV}$ , which they attributed to the instrument artifact (Lavvas et al., 2011; Arridge et al., 2009).

### 3.2. Volume Emission rates

Using the photoelectron flux  $\phi(Z, E)$  obtained in equation (1), the volume excitation rate for  $\text{N}_2$  emissions is calculated as

$$V_i(Z) = n(Z) \int_{E_{th}}^E \phi(Z, E) \sigma_i(E) dE \quad (3)$$

where  $n(Z)$  is the density of  $\text{N}_2$  at altitude  $Z$  and  $\sigma_i(E)$  is the electron impact cross section for the  $i$ th state at energy  $E$ , for which the threshold is  $E_{th}$ . Figure 5

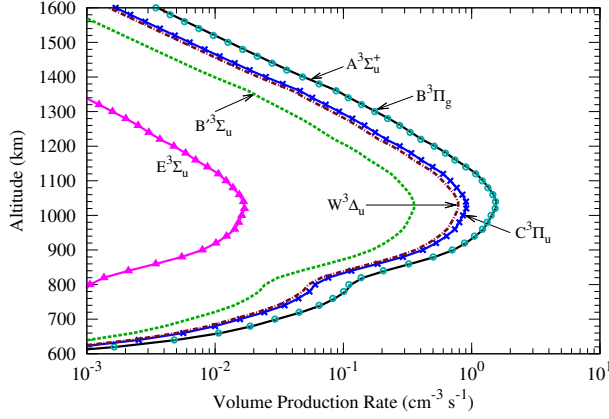


Figure 5: Calculated volume production rate of different triplet states of N<sub>2</sub> due to photoelectron impact at SZA=60° for SEE solar EUV flux.

shows the volume excitation rates for N<sub>2</sub> triplet states (*A*, *B*, *C*, *W*, *B'*, and *E*) by photoelectron impact excitation. The production rates for all the states peak around 1025 km, which is ~ 25 km higher than the calculated peak altitude of ~1000 km of Stevens et al. (2011). This difference in height of peak production might due to the different treatment of altitude dependence of photoelectrons in the two models.

The N<sub>2</sub> triplet *E*, *C*, *W*, and *B'* states populate the *B* state, which in turn radiate to the state *A* (First Positive band). Further the interstate cascading  $B^3\Pi_g \rightleftharpoons A^3\Sigma_u^+$  and  $B^3\Pi_g \rightleftharpoons W^3\Delta_u$  are also important in populating the *B* level (Cartwright et al., 1971; Cartwright, 1978; Jain and Bhardwaj, 2011; Bhardwaj and Jain, 2011). To calculate the total population of different vibrational levels of state *A*, we solve the equations for statistical equilibrium based on the formulation of Cartwright (1978). Contributions of cascading from higher triplet states and interstate cascading and quenching by atmosphere constituents are included in the calculation. At a specified altitude, for a vibrational level  $\nu$  of a state  $\alpha$ , the population is determined using the statistical equilibrium equation

$$V^\alpha q_{0\nu} + \sum_{\beta} \sum_s A_{s\nu}^{\beta\alpha} n_s^\beta = \{K_{q\nu}^\alpha + \sum_{\gamma} \sum_r A_{r\nu}^{\alpha\gamma}\} n_\nu^\alpha \quad (4)$$

where,  $V^\alpha$  is electron impact volume excitation rate (cm<sup>-3</sup> s<sup>-1</sup>) of state  $\alpha$ ;  $q_{0\nu}$  is Franck-Condon factor for the excitation from ground level to  $\nu$  level of state  $\alpha$ ;  $A_{s\nu}^{\beta\alpha}$  is transition probability (s<sup>-1</sup>) from state  $\beta(s)$  to  $\alpha(\nu)$ ;  $K_{q\nu}^\alpha$  is total electronic quenching frequency (s<sup>-1</sup>) of level  $\nu$  of state  $\alpha$  by all the gases defined as:  $\sum_l K_{q(l)\nu}^\alpha \times n_l$ , where,

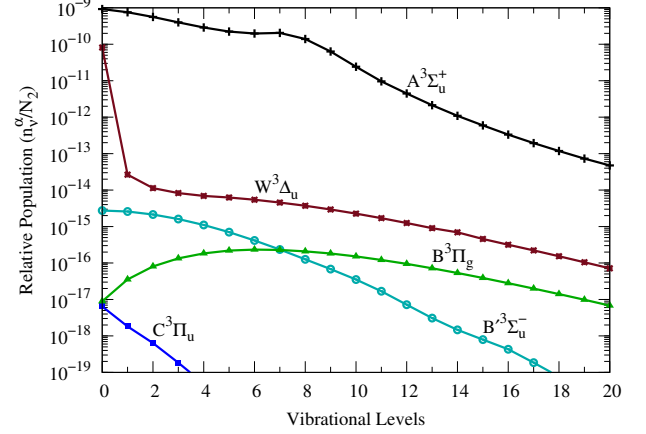


Figure 6: Calculated relative vibrational population of the various triplet states of N<sub>2</sub> at an altitude of 1100 km at SZA=60° using SEE solar flux.

$K_{q(l)\nu}^\alpha$  is the quenching rate coefficient of level  $\nu$  of state  $\alpha$  by the gas  $l$  of density  $n_l$ ;  $A_{r\nu}^{\alpha\gamma}$  is transition from level  $\nu$  of state  $\alpha$  to vibrational level  $r$  of state  $\gamma$ ;  $n$  is density (cm<sup>-3</sup>);  $\alpha, \beta$ , and  $\gamma$  are electronic states; and  $s$  and  $r$  are source and sink vibrational levels, respectively.

While calculating the cascading from *C* state, we have accounted for predissociation. The *C* state predissociates approximately half the time (this is an average value for all vibrational levels of the *C* state; excluding  $\nu = 0, 1$ , which do not predissociate at all) (cf. Daniell and Strickland, 1986). In Earth's airglow the N<sub>2</sub>(*A*) levels get effectively quenched by atomic oxygen and the abundance of O increases with increase in altitude. Titan atmosphere is N<sub>2</sub> dominated with small amount of CH<sub>4</sub>. The quenching rates for different vibrational levels of N<sub>2</sub> triplet states by N<sub>2</sub> are adopted from Morrill and Benesch (1996) and by CH<sub>4</sub> is taken from Clark and Setser (1980).

Figure 6 shows the population of different vibrational levels of triplet states of N<sub>2</sub> relative to the ground state at 1100 km. We found that the effect of quenching is negligible on the vibrational population. Stevens et al. (2011) have taken the vibrational population of VK band up to 10 vibrational levels and the population of vibrational level 11 is taken as 44% of that for  $\nu' = 10$ . In our model, the vibrational population is considered up to  $\nu' = 20$  levels. Our calculated population for  $\nu' = 11$  level is ~40% of the  $\nu' = 10$  level.

After calculating the steady state density of different vibrational levels of excited triplet states of N<sub>2</sub>, the volume emission rate  $V_{\nu'\nu''}^{\alpha\beta}$  of a vibration band  $\nu' \rightarrow \nu''$  can



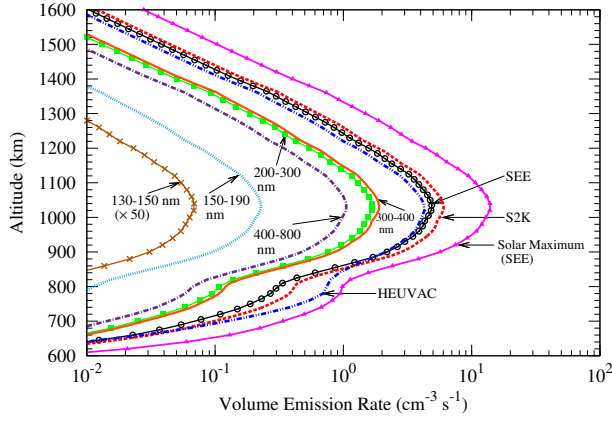


Figure 7: Volume emission rate of total N<sub>2</sub> VK band along with the emission rates of VK band in different wavelength regions calculated using SEE solar flux model at SZA = 60°. Total N<sub>2</sub> VK band emission rate of 130–150 nm band is plotted after multiplying by a factor of 50. Emission rate profiles for SOLAR2000 (S2K) and HEUVAC model solar fluxes and in solar maximum (for SEE solar EUV flux) are also shown.

be obtained using

$$V_{\nu'\nu''}^{\alpha\beta} = n_{\nu'}^{\alpha} \times A_{\nu'\nu''}^{\alpha\beta} \quad (\text{cm}^{-3} \text{ s}^{-1}) \quad (5)$$

where  $n_{\nu'}^{\alpha}$  is the density of vibrational level  $\nu'$  of state  $\alpha$ , and  $A_{\nu'\nu''}^{\alpha\beta}$  is the transition probability ( $\text{s}^{-1}$ ) for the transition from the  $\nu'$  level of state  $\alpha$  to the  $\nu''$  level of state  $\beta$ .

Figure 7 shows the volume emission rates for the VK band. The N<sub>2</sub> VK band span wavelength range from FUV to visible, and some transitions even emit at wavelength more than 1000 nm. Figure 7 also shows the emission rates of VK bands in FUV and visible wavelengths. Volume emission rates for VK bands in the wavelength range 400–800, 300–400, 200–300, and 150–200 nm are 22%, 38%, 35%, and 4.5% of the total VK band emission rate. Contribution of VK band emissions in the 130–150 nm wavelength range is very small (0.02%). In the visible and near infrared range (400–800 nm), the main contribution comes from the emissions between 400 and 500 nm, which comprises around 73% of the VK visible emission band. Our calculated total VK band volume emission rate is in good agreement with that of Stevens et al. (2011).

Figure 8 shows the prominent VK band transition in ultraviolet region. VK (0, 5), (0, 6), and (0, 7) bands (between 200–300 nm) have been observed on Mars by SPICAM/Mars Express (Leblanc et al., 2006, 2007). In the 150–200 nm region, VK (5, 0), (6, 0), (7, 0), (8, 0), and (9, 0) bands are reported for the first time in the

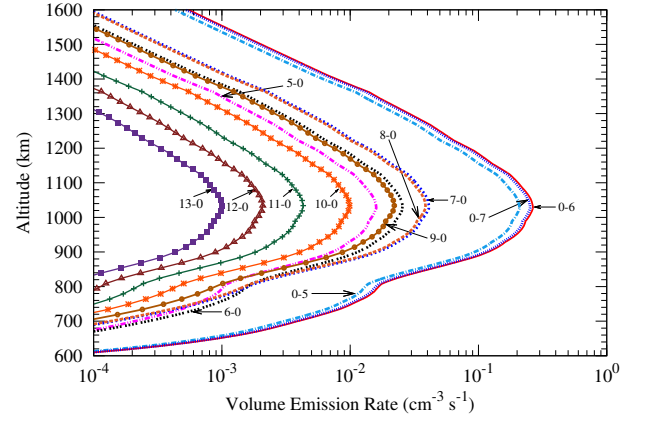


Figure 8: Volume emission rate profiles of prominent transitions of N<sub>2</sub> VK band emission calculated using SEE solar flux model at SZA = 60°.

dayglow of Titan (Stevens et al., 2011). The production rates in these two wavelength band regions, 150–200 and 200–300 nm, differ by about an order of magnitude but the altitude of peak production (1025 km) remains the same for all the VK band emissions (Figure 7).

The volume emission rates are vertically-integrated to calculate the overhead intensities. Table 1 shows the total overhead intensity for Vegard-Kaplan ( $A \rightarrow X$ ), First positive ( $B \rightarrow A$ ), Second Positive ( $C \rightarrow B$ ), Herman-Kaplan ( $E \rightarrow A$ ),  $E \rightarrow B$ , Reverse First Positive ( $A \rightarrow B$ ), and  $E \rightarrow C$  triplet bands of N<sub>2</sub> at SZA=60°. Since the VK band spans a wide range of electromagnetic spectrum, from FUV to visible wavelengths, we also present in Table 1 the overhead intensities in different wavelength regions of VK bands. Emissions in the 300–400 nm constitute a major fraction of the total VK band emission followed closely by emissions in the 200–300 nm band, with contributions of around 38% and 35%, respectively. The 150–200 nm emission band contributes around 4.5% to the total VK band intensity. Contribution of visible wavelength region (400–800 nm) is also significant (22%) in the total VK band intensity, in which wavelength region 400–500 nm contributes ~16% of the total VK band intensity or 73% of total visible band emission.

Table 2 shows the overhead intensity for all the vibrational levels of N<sub>2</sub> VK bands calculated using SEE solar EUV flux on 23 June 2009 at SZA = 60°. The VK (0, 6) emission (at 276.2 nm) is the strongest emission in the VK band system having an overhead intensity of ~7 R, which is around 5% of the total VK band intensity and comprises around 15% of VK band emissions in the 200–300 nm range. The VK (0, 6) band has

been observed on Mars (Leblanc et al., 2007; Jain and Bhardwaj, 2011). In the dayglow spectrum of Titan VK (7, 0) transition is the strongest emission observed by Cassini UVIS. For the VK (7, 0) band the model calculated overhead intensity is 1.1 R, which is 0.8% of the total VK band intensity.

The calculated overhead intensities of N<sub>2</sub> First Positive (1P) transitions are presented in Table 3. Prominent transitions in this band lies above 600 nm. The 1P (1, 0) emission at 888.3 nm is the brightest followed by (0, 0) emission at 1046.9 nm, which contribute around 13% and 9%, respectively, to the total 1P emission. Emissions between 600 and 800 nm wavelength consist of about 50% of the total 1P band system. The calculated overhead intensities of Second Positive (2P) band transitions are presented in Table 4. Major portion of 2P band emission lies in wavelengths between 300 and 400 nm, which is more than 90% of the total 2P band overhead intensity. Prominent emissions in the 2P band system are (0, 0), (0, 1), (0, 2), and (1, 0) transitions, having overhead intensities of around 6.5, 4.5, 1.8, and 1.7 R, thus contributing around 34, 24, 9, and 9%, respectively, to the total 2P emission.

Tables 5 and 6 show the calculated overhead intensities of Wu-Benesch ( $W \rightarrow B$ ) and  $B' \rightarrow B$  band emissions, respectively. Most of the emissions in  $W \rightarrow B$  band are in infrared region with a little or negligible contribution from emissions below 800 nm. Similar is the case in  $B' \rightarrow B$  band system. Table 7 shows the calculated overhead intensities of Herman-Kaplan ( $E \rightarrow A$ ),  $E \rightarrow B$ , and  $E \rightarrow C$  bands of N<sub>2</sub>, and Table 8 shows the overhead intensities of Reverse First Positive (R1P) band emissions. Prominent emissions in the R1P band system are in infrared region, with (9, 0) emission being the strongest having the overhead intensity of 1.9 R, which is around 9% of the total R1P emission.

Stevens et al. (2011) suggested that N<sub>2</sub> VK (8, 0) emission near 165.4 nm and (11, 0) band near 156.3 nm could have been misidentified as CI 165.7 and 156.1 nm emissions by Ajello et al. (2008). Also, the VK (10, 0) band could be the emission near 159.2 nm, which is reported as mystery feature by Ajello et al. (2008). We calculated the overhead intensities of CI 165.7 and 156.1 nm emissions due to electron impact dissociative excitation of CH<sub>4</sub> by using the emission cross sections from Shirai et al. (2002). The model calculated overhead intensities of CI 156.1 and 165.7 nm emissions are  $1.6 \times 10^{-3}$  and  $3.7 \times 10^{-3}$  R, respectively, which are about 2 orders of magnitude lower than the VK (8, 0) and VK (11, 0) bands intensities (see Table 2). We also estimated the solar scattered intensities for CI 165.7 and 156.1 nm using the density of atomic carbon from the

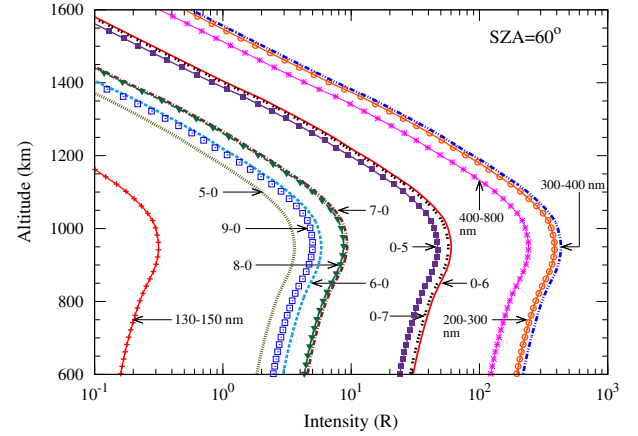


Figure 9: Limb profiles of prominent transitions of N<sub>2</sub> VK bands calculated using SEE solar flux model at SZA = 60°. Limb profiles of N<sub>2</sub> VK band in different wavelength regions (130–150, 200–300, 300–400, and 400–800 nm) are also shown.

model of Krasnopolsky (2010) and  $g$ -factor values of  $7.21 \times 10^{-6}$  and  $2 \times 10^{-5} \text{ sec}^{-1}$ , respectively, at 1 AU. The overhead intensities of CI 156.1 and 165.7 nm due to solar fluorescence are an order of magnitude lower ( $1.98 \times 10^{-4}$  and  $5.5 \times 10^{-4}$  R, respectively) than that due to photoelectron excitation. The difference of 2 to 3 orders of magnitude between intensities of (8, 0) and (11, 0) VK bands and CI line emissions suggest that bands near 156.1 and 165.4 nm might have been misidentified by Ajello et al. (2008), as reported by Stevens et al. (2011).

The calculated band emission rate is integrated along the line of sight at a projected distance from the centre of Titan to obtain limb profile. Figure 9 shows the calculated limb intensities of the prominent VK band emissions in ultraviolet region. Limb intensities of VK bands in different wavelength regions are also shown in Figure 9. The altitude of maximum limb intensity is around 950 km for all the transitions, slightly higher than the calculated N<sub>2</sub> VK peak of Stevens et al. (2011) of ~928 km. Figure 10 shows the limb intensity of total VK band, which peaks at ~950 km, with a value of around 1.1 kR. Limb intensities calculated at different solar zenith angle are also shown in Figure 10. The main effect of SZA is on the altitude of peak limb intensity and intensity at the peak; lower the value of SZA, the deeper the peak of the limb profile with higher intensity, which is due to the penetration of solar EUV at lower altitudes in the atmosphere. For SZA = 0°, the calculated peak limb intensity is 2.2 kR at an altitude of 892 km, whereas at SZA = 80°, the peak limb intensity is 0.4 kR at an altitude of 1050 km. Above 1200 km



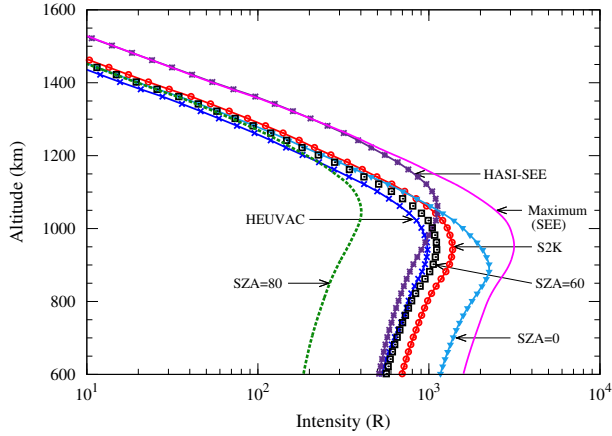


Figure 10: Limb profiles of total  $N_2$  VK bands at three different solar zenith angles (0, 60, and 80 degrees) calculated using SEE solar EUV flux model. Limb profiles calculated using S2K and HEUVAC models, and in solar maximum condition (for SEE solar flux) are shown for  $SZA = 60^\circ$ . Limb intensity profile calculated using HASI  $N_2$  density and SEE solar EUV flux is also shown for  $SZA = 60^\circ$ .

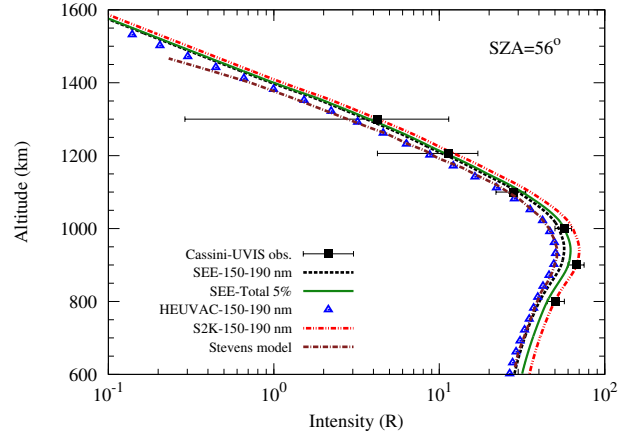


Figure 11: Calculated limb profiles of  $N_2$  VK 150–190 nm wavelength range emissions on 23 June 2009 for SEE, S2K, and HEUVAC solar EUV flux models at  $SZA=56^\circ$ , along with the Cassini UVIS observed limb intensity and model profile of Stevens et al. (2011). Limb profile obtained by taking 5% of the total  $N_2$  VK band intensity is also shown.

the effect of solar zenith angle is not seen in the limb intensities.

As mentioned earlier,  $N_2$  VK bands were observed for the first time in the dayglow of Titan by Cassini UVIS in the 150–190 nm wavelength band (Stevens et al., 2011). For comparing our calculated limb profiles with UVIS observation we have run our model at the solar zenith angle of  $56^\circ$ . Stevens et al. (2011) in their calculation assumed that VK bands in the 150–190 nm range corresponds to 5% of total VK band emission. Figure 11 shows the calculated limb intensity of VK bands in the 150–190 nm region by taking 5% of the total VK band intensity, and also by adding the individual bands which lie in the 150–190 nm wavelength region. The calculated limb intensity of Stevens et al. (2011) is also shown in Figure 11 along with the Cassini–observed limb intensity of VK band in 150–190 nm region taken from Stevens et al. (2011). We found that VK band emission in the wavelength region 150–190 nm corresponds to 4.5% of the total VK band intensity (see Table 1). Our calculated limb intensity is in good agreement with the UVIS observation. The calculated altitude of peak VK emission also agrees well with the observation within the observational uncertainty of 15% (Stevens et al., 2011). Our calculated limb intensities are slightly higher ( $\sim 10\%$ ) than those calculated by Stevens et al. (2011). Altitude of emission peak is in good agreement in both calculations and is consistent with that of the observed emission peak. Overall good agreement between calculated and observed emission

shows that the VK band intensity can be explained by taking the photoelectron impact excitation source alone.

## 4. Effect of various model input parameters

### 4.1. Effect of solar EUV flux model

To access the effect of solar EUV flux on the calculated limb intensity we use the solar EUV flux on 23 June 2009 from SOLAR2000 (S2K) v.2.36 model of Tobiska (2004) and HEUVAC model of Richards et al. (2006). As discussed in Section 2, the solar flux at wavelengths below 60 nm is higher in the S2K model (cf. Figure 1). The effect of higher flux at shorter wavelengths is clearly seen in the photoelectron flux calculations, where the flux calculated using S2K model is higher than that calculated using SEE solar EUV flux (cf. Figure 3). While the HEUVAC solar flux is smaller than the SEE solar flux at wavelengths higher than 15 nm, at wavelengths below 15 nm the HEUVAC solar flux is higher than SEE flux. Higher EUV fluxes at shorter wavelength would cause higher photoelectron flux at higher energies ( $>60$  eV) (see Figure. 3).

Volume emission rates of total VK band calculated using S2K and HEUVAC solar flux models are shown in Figure 7. The emission rate calculated using S2K model is  $\sim 23\%$  higher than that calculated using SEE solar EUV flux. At the emission peak and above, volume emission rate calculated using HEUVAC model is around 14% smaller than that calculated using SEE solar flux. However, below the emission peak, the vol-

ume emission rate calculated using HEUVAC model becomes higher than that calculated using SEE model due to the larger photoelectron fluxes at higher energies (cf. Figure 3). At the lower peak, volume emission rate calculated using HEUVAC model is around 2.5 times higher than that calculated using SEE solar EUV flux.

Figures 10 and 11 show the limb intensity of VK band calculated using S2K and HEUVAC solar flux models. Limb intensities calculated using S2K solar EUV flux model are slightly higher than the observed values whereas intensities calculated using SEE and HEUVAC solar fluxes and model predicted intensity of Stevens et al. (2011) are lower than the observed values; but all model calculations are in good agreement with the observation within the observation and model uncertainties. The height of peak emission rate (Figure 7) and altitude of peak limb intensity (Figures 10 and 11) are unaffected by change in input solar EUV flux model.

By changing the solar EUV flux in model, maximum variation at peak intensity is around 40%. Since uncertainty in various solar EUV flux itself varies differently for different solar EUV flux, e.g., for SEE observations uncertainty is around 10–20% (Woods et al., 2005), uncertainty in HEUVAC model depend on the uncertainties in the F74113 reference spectrum and it could be 15–30% (Richards et al., 2006). Hence, based on the calculations carried out in the present paper, it is difficult to suggest a preferred solar flux model. However, since HEUVAC and S2K depend on various proxies, while SEE solar EUV flux is based on actual observation and is available online ([http://lasp.colorado.edu/see/13\\_data\\_page.html](http://lasp.colorado.edu/see/13_data_page.html)) it is preferable to use SEE solar EUV flux.

#### 4.2. Effect of solar cycle

The N<sub>2</sub> VK band emissions reported by Stevens et al. (2011) are for low solar activity condition (F10.7 = 68, on 23 June 2009). To calculate the emission intensity during solar maximum we have run our model for solar EUV flux on 30 January 2002 (F10.7 = 245) measured by SEE at solar zenith angle 60°. Model atmosphere remains the same for the solar maximum calculation. Figure 7 shows the volume emission rate of total N<sub>2</sub> VK band for solar maximum condition. At the altitude where emission rate peaks, the calculated emission rate for solar maximum condition is a factor of ~2.8 higher than that for solar minimum condition. Altitude of peak emission rate remains the same for both low and high solar activity condition since the model atmosphere is same. Overhead intensities of individual transition in various triplet states are also a factor of 2.8 to 2.9 higher for the solar maximum condition (cf. Table 1). Similar

increase of around factor of 2.8 can be seen in limb intensity of total N<sub>2</sub> VK band for solar maximum condition (see Figure 9). We have also run our model for the moderate solar activity condition using the SEE solar EUV flux for 20 June 2002 (F10.7 = 150) at SZA = 60°. Model atmosphere remains the same. Table 1 shows the calculated overhead intensities of various triplet states during the moderate solar activity condition, which are a factor of 2 higher than those calculated during solar minimum condition.

#### 4.3. Effect of model atmosphere

Huygens Atmospheric Structure Instrument (HASI) measured the density profile of N<sub>2</sub> in Titan’s atmosphere (Fulchignoni et al., 2005). In our calculations we have used the density profile of N<sub>2</sub> observed by HASI, but reduced by a factor of 3.1 to be consistent with N<sub>2</sub> densities measured by Ion and Neutral Mass Spectrometer (INMS) (De La Haye et al., 2007) at 950 km. This reduction is also required for the better agreement in the UVIS-observed and calculated emission peak altitudes. To see the effect of higher N<sub>2</sub> density on emission intensities, we have run our model using the original unscaled HASI N<sub>2</sub> density profile keeping the other model input parameters same. Figure 10 shows the limb profile of N<sub>2</sub> VK band calculated using HASI N<sub>2</sub> density. The altitude of the peak emission is situated at 1052 km with a value of ~1.12 kR when HASI N<sub>2</sub> density profile is used. Thus, the calculated altitude of peak emission is around 100 km higher than that calculated by using reduced (by a factor of 3.1) N<sub>2</sub> density, but the intensity of emission at the peak remains the same (1.11 kR).

### 5. Summary

A model for the production of N<sub>2</sub> triplet band emissions in the dayglow of Titan is developed. We have used the Analytical Yield Spectra technique to calculate the steady state photoelectron flux, which is compared with the Cassini CAPS observed photoelectron flux. The calculated photoelectron flux is in good agreement with the observed spectrum in the 6–60 eV energy range. Volume production rates of various triplet states of N<sub>2</sub> have been calculated. Population of any given level of triplet states has been calculated considering direct electron impact excitation and quenching as well as cascading from higher triplet states in statistical equilibrium condition. Volume emission rates are calculated and vertically-integrated to calculate the overhead intensities of Vegard-Kaplan in various wavelength regions, viz., 130–150, 150–200, 200–300, 300–400, and 400–800 nm, which are given in Table 1. In

addition, the vertical-integrated intensities of First Positive, Second Positive, Wu-Benesch,  $B' \rightarrow B$ ,  $E \rightarrow C$ ,  $E \rightarrow B$ ,  $E \rightarrow A$ , and Reverse First Positive bands of  $N_2$ , are also calculated and presented in Table 1 along with their contributions in different wavelength regions. Vertically-integrated overhead intensities of various vibrational transitions in triplet states are presented in Tables 2 to 8.

The calculated volume emission rates are integrated along the line of sight to calculate the limb intensity of total VK band. Limb profiles of various prominent transitions of VK band are also calculated and presented in Figure 9. The VK band in the wavelength region 200–400 nm contribute around 73% of the total VK band intensity, followed by the VK band in visible region (400–800 nm) which contributes around 22%. The calculated limb intensity profile of VK 150–190 nm band is in good agreement with the recent Cassini UVIS-observed profile. We found that the observed intensity of VK bands can be explained by the photoelectron impact excitation alone (Stevens et al., 2011). The effect of change in solar zenith angle is seen in the altitude of peak emission as well as intensity at the emission peak. Variation in the SZA from  $0^\circ$  to  $80^\circ$  resulted in  $\sim 18\%$  upward shift in the altitude of emission peak, while the limb intensity at the peak decreased by a factor of 5.5. Our calculation suggests that intensity of CI 156.1 and 165.7 nm emissions due to photoelectron impact dissociative excitation of  $CH_4$  and fluorescence scattering of solar lines by carbon in Titan's atmosphere are a few orders of magnitude smaller than the  $N_2$  VK bands 11–0 (156.3 nm) and 8–0 (165.4 nm) emission intensities, respectively.

We have also made a detailed study on the effect of solar EUV flux models on the  $N_2$  triplet band emission intensities which is a step further to the calculations of Stevens et al. (2011). Emission intensities calculated by using the S2K model are around 23% higher than that calculated using the SEE solar flux. The limb intensity at peak calculated using the HEUVAC model is around 13% smaller than that calculated using SEE solar flux. The calculated intensities for moderate ( $F_{10.7} = 150$ ) and high ( $F_{10.7} = 240$ ) solar activity conditions are about a factor of 2 and 2.8, respectively, higher than those calculated during solar minimum ( $F_{10.7} = 68$ ) condition. Calculations are also carried out taking the HASI-observed  $N_2$  density in the model atmosphere. Due to higher  $N_2$  density in the HASI observation by a factor of 3.1, the altitude of peak emission shifted upwards by 100 km; however, the intensity at the peak remains the same.

The calculations presented in this paper will help in

understanding the production of  $N_2$  VK and other triplet band dayglow emissions on Titan as well as in other  $N_2$ -containing planetary atmospheres.

## Acknowledgement

Sonal Kumar Jain was supported by Senior Research Fellowship of ISRO during the period of this work.

## References

- Ajello, J. M., Gustin, J., Stewart, I., Larsen, K., Esposito, L., Pryor, W., McClintock, W., Stevens, M. H., Malone, C. P., Dziczek, D., 2008. Titan airglow spectra from the Cassini Ultraviolet Imaging Spectrograph: FUV disk analysis. *Geophys. Res. Lett.* 35, L06102. doi:10.1029/2007GL032315.
- Ajello, J. M., Stevens, M. H., Stewart, I., Larsen, K., Esposito, L., Colwell, J., McClintock, W., Holsclaw, G., Gustin, J., Pryor, W., 2007. Titan airglow spectra from Cassini Ultraviolet Imaging Spectrograph (UVIS): EUV analysis. *Geophys. Res. Lett.* 34, L24204. doi:10.1029/2007GL031555.
- Arridge, C. S., Gilbert, L. K., Lewis, G. R., Sittler, E. C., Jones, G. H., Kataria, D. O., Coates, A. J., Young, D. T., 2009. The effect of spacecraft radiation sources on the electron moments from the Cassini CAPS electron spectrometer. *Planet. Space Sci.* 57, 854 – 869. doi:10.1016/j.pss.2009.02.011.
- Avakyan, S. V., Il'in, R. N., Lavrov, V. M., Ogurtsov, G. N., 1998. In: Avakyan, S. V. (Ed.), *Collision Processes and Excitation of UV Emission from Planetary Atmospheric Gases: A Handbook of Cross Sections*. Gordon and Breach science publishers.
- Bhardwaj, A., 1999. On the role of solar EUV, photoelectrons, and auroral electrons in the chemistry of  $C(^1D)$  and the production of CI 1931 Å in the inner cometary coma: A case for comet P/Halley. *J. Geophys. Res.* 104, 1929 – 1942. doi:10.1029/1998JE900004.
- Bhardwaj, A., 2003. On the solar EUV deposition in the inner coma of comets with large gas production rates. *Geophys. Res. Lett.* 30 (24), 2244. doi:10.1029/2003GL018495.
- Bhardwaj, A., Haider, S. A., Singhal, R. P., 1990. Auroral and photoelectron fluxes in cometary ionospheres. *Icarus* 85, 216 – 228. doi:10.1016/0019-1035(90)90112-M.
- Bhardwaj, A., Haider, S. A., Singhal, R. P., 1996. Production and emissions of atomic carbon and oxygen in the inner coma of comet 1P/Halley: Role of electron impact. *Icarus* 120, 412 – 430. doi:10.1006/icar.1996.0061.
- Bhardwaj, A., Jain, S. K., 2009. Monte Carlo model of electron energy degradation in a  $CO_2$  atmosphere. *J. Geophys. Res.* 114, A11309. doi:10.1029/2009JA014298.
- Bhardwaj, A., Jain, S. K., 2011. Calculations of  $N_2$  triplet states vibrational populations and band emissions in venusian dayglow. *Icarus* 217, 752 – 758. doi:10.1016/j.icarus.2011.05.026.
- Bhardwaj, A., Michael, M., 1999a. Monte Carlo model for electron degradation in  $SO_2$  gas: cross sections, yield spectra and efficiencies. *J. Geophys. Res.* 104 (10), 24713 – 24728. doi:10.1029/1999JA900283.
- Bhardwaj, A., Michael, M., 1999b. On the excitation of Io's atmosphere by the photoelectrons: Application of the analytical yield spectrum of  $SO_2$ . *Geophys. Res. Lett.* 26, 393 – 396. doi:10.1029/1998GL090320.
- Bhardwaj, A., Raghuram, S., 2011. Coupled Chemistry-Emission Model for Atomic Oxygen Green and Red-doublet Emissions in Comet C/1996 B2 Hyakutake. *Astrophys. J.* In press. doi:10.1088/0004-637X/745/1/1

- Bhardwaj, A., Singhal, R. P., 1990. Auroral and dayglow processes on Neptune. *Indian Journal of Radio and Space Physics* 19, 171 – 176.
- Bhardwaj, A., Singhal, R. P., 1993. Optically thin H Lyman alpha production on outer planets: Low-energy proton acceleration in parallel electric fields and neutral H atom precipitation from ring current. *J. Geophys. Res.* 98 (A6), 9473 – 9481. doi: 10.1029/92JA02400.
- Broadfoot, A., Hatfield, D., Anderson, E., Stone, T., Sandel, B., Gardner, J., Murad, E., Knecht, D., Pike, C., Viereck, R., 1997. N<sub>2</sub> triplet band systems and atomic oxygen in the dayglow. *J. Geophys. Res.* 102 (A6), 11567 – 11584. doi:10.1029/97JA00771.
- Broadfoot, A. L., Sandel, B. R., Shemansky, D. E., Holberg, J. B., Smith, G. R., Strobel, D. F., McConnell, J. C., Kumar, S., Hunten, D. M., Atreya, S. K., Donahue, T. M., Moos, H. W., Bertaux, J. L., Blamont, J. E., Pomphrey, R. B., Linick, S., April 1981. Extreme ultraviolet observations from Voyager 1 encounter with Saturn. *Science* 212, 206 – 211. doi:10.1126/science.212.4491.206.
- Brown, R. H. et al., 2004. The Cassini Visual and Infrared Mapping Spectrometer (VIMS) Investigation. *Space Science Reviews* 115, 111–168. doi:10.1007/s11214-004-1453-x.
- Cartwright, D., Trajmar, S., Williams, W., 1971. Vibrational population of the  $A^3\Sigma_u^+$  and  $B^3\Pi_g$  states of N<sub>2</sub> in normal auroras. *J. Geophys. Res.* 76 (34), 8368 – 8377. doi:10.1029/JA076i034p08368.
- Cartwright, D. C., 1978. Vibrational populations of the excited state of N<sub>2</sub> under auroral condition. *J. Geophys. Res.* 83 (A2), 517 – 321. doi:10.1029/JA083iA02p00517.
- Clark, W. G., Setser, D. W., 1980. Energy transfer reactions of N<sub>2</sub> ( $A^3\Sigma_u^+$ ). 5. Quenching by hydrogen halides, methyl halides, and other molecules. *J. Phys. Chem.* 84 (18), 2225 – 2233.
- Daniell, R., Strickland, D., 1986. Dependence of auroral middle UV emissions on the incident electron spectrum and neutral atmosphere. *J. Geophys. Res.* 91 (A1), 321 – 327. doi: 10.1029/JA091iA01p00321.
- De La Haye, V., Waite, J. H., Johnson, R. E., Yelle, R. V., Cravens, T. E., Luhmann, J. G., Kasprzak, W. T., Gell, D. A., Magee, B., Leblanc, F., Michael, M., Jurac, S., Robertson, I. P., Jul. 2007. Cassini Ion and Neutral Mass Spectrometer data in Titan's upper atmosphere and exosphere: Observation of a suprathermal corona. *J. Geophys. Res.* 112, A07309. doi:10.1029/2006JA012222.
- Fulchignoni, M. et al., 2005. In situ measurements of the physical characteristics of Titan's environment. *Nature* 438, 785–791. doi: 10.1038/nature04314.
- Gilmore, F. R., Laher, R. R., Espy, P. J., 1992. Franck-Condon factors, r-centroids, electronic transition moments, and Einstein coefficients for many nitrogen and oxygen band systems. *J. Phys. Chem. Ref. Data* 21, 1005 – 1107. doi:10.1063/1.555910.
- Huebner, W. F., Keady, J. J., Lyon, S. P., 1992. Solar photorates for planetary atmospheres and atmospheric pollutants. *Astrophys. Space Sci.* 195 (1), 1 – 289. doi:10.1007/BF00644558.
- Itikawa, Y., 2006. Cross sections for electron collisions with nitrogen molecules. *J. Phys. Chem. Ref. Data* 35 (1), 31 – 53. doi: 10.1063/1.1937426.
- Jackman, C., Garvey, R., Green, A., 1977. Electron impact on atmospheric gases, I. Updated cross sections. *J. Geophys. Res.* 82 (32), 5081 – 5090. doi:10.1029/JA082i032p05081.
- Jain, S. K., Bhardwaj, A., 2011. Model calculation of N<sub>2</sub> Vegard-Kaplan band emissions in Martian dayglow. *J. Geophys. Res.* 116, E07005. doi:10.1029/2010JE003778.
- Krasnopolsky, V. A., 2010. The photochemical model of Titan's atmosphere and ionosphere: A version without hydrodynamic escape. *Planetary and Space Science* 58, 1507 – 1515. doi: 10.1016/j.pss.2010.07.010.
- Lavvas, P., Galand, M., Yelle, R. V., Heays, A. N., Lewis, B. R., Lewis, G. R., Coates, A. J., 2011. Energy deposition and primary chemical products in Titan's upper atmosphere. *Icarus* 213, 233 – 251. doi:10.1016/j.icarus.2011.03.001.
- Lean, J. L., Woods, T. N., Eparvier, F. G., Meier, R. R., Strickland, D. J., Correia, J. T., Evans, J. S., 2011. Solar extreme ultraviolet irradiance: Present, past, and future. *J. Geophys. Res.* 116, A01102. doi:10.1029/2010JA015901.
- Leblanc, F., Chaufray, J. Y., Bertaux, J. L., 2007. On Martian nitrogen dayglow emission observed by SPICAM UV spectrograph/Mars Express. *Geophys. Res. Lett.* 34, L02206. doi: 10.1029/2006GL0284.
- Leblanc, F., Chaufray, J. Y., Lilensten, J., Witasse, O., Bertaux, J.-L., 2006. Martian dayglow as seen by the SPICAM UV spectrograph on Mars Express. *J. Geophys. Res.* 111, E09S11. doi: 10.1029/2005JE002664.
- Meier, R., 1991. Ultraviolet spectroscopy and remote sensing of the upper atmosphere. *Space Science Reviews* 58, 1–185. doi: 10.1007/BF01206000.
- Michael, M., Bhardwaj, A., 1997. On the dissociative ionization of SO<sub>2</sub> in the Io's atmosphere. *Geophys. Res. Lett.* 24, 1971 – 1974. doi:10.1029/97GL02056.
- Morrill, J., Benesch, W., 1996. Auroral N<sub>2</sub> emissions and the effect of collisional processes on N<sub>2</sub> triplet state vibrational populations. *J. Geophys. Res.* 101 (A1), 261 – 274. doi:10.1029/95JA02835.
- Porco, C. C., West, R. A., Squyres, S., McEwen, A., Thomas, P., Murray, C. D., Del Genio, A., Ingersoll, A. P., Johnson, T. V., Neukum, G., Veverka, J., Dones, L., Brahic, A., Burns, J. A., Haemmerle, V., Knowles, B., Dawson, D., Roatsch, T., Beurle, K., Owen, W., 2004. Cassini Imaging Science: Instrument characteristics And anticipated scientific investigations at Saturn. *Space Sci. Rev.* 115, 363 – 497. doi:10.1007/s11214-004-1456-7.
- Richards, P. G., Woods, T. N., Peterson, W. K., 2006. HEUVAC: A new high resolution solar EUV proxy model. *Adv. Space Res.* 37 (2), 315 – 322. doi:10.1016/j.asr.2005.06.031.
- Shemansky, D. E., Stewart, A. I. F., West, R. A., Esposito, L. W., Hallett, J. T., Liu, X., 2005. The Cassini UVIS stellar probe of the Titan atmosphere. *Science* 308, 978 – 982. doi: 10.1126/science.1111790.
- Shirai, T., Tabata, T., Tawara, H., Itikawa, Y., 2002. Analytic cross sections for electron collisions with hydrocarbons: CH<sub>4</sub>, C<sub>2</sub>H<sub>6</sub>, C<sub>2</sub>H<sub>4</sub>, C<sub>2</sub>H<sub>2</sub>, C<sub>3</sub>H<sub>8</sub>, and C<sub>3</sub>H<sub>6</sub>. *At. Data Nucl. Data Tables* 80, 147 – 204. doi:10.1006/adnd.2001.0878.
- Singhal, R. P., Bhardwaj, A., 1991. Monte Carlo simulation of photoelectron energization in parallel electric fields: Electrolow on Uranus. *J. Geophys. Res.* 96, 15963 – 15972. doi: 10.1029/90JA02749.
- Singhal, R. P., Haider, S. A., 1984. Analytical Yield Spectrum approach to photoelectron fluxes in the Earth's atmosphere. *J. Geophys. Res.* 89 (A8), 6847 – 6852. doi:10.1029/JA089iA08p06847.
- Singhal, R. P., Jackman, C., Green, A. E. S., 1980. Spatial aspects of low and medium energy electron degradation in N<sub>2</sub>. *J. Geophys. Res.* 85 (A3), 1246 – 1254. doi:10.1029/JA085iA03p01246.
- Stevens, M. H., 2001. The EUV airglow of Titan: Production and loss of N<sub>2</sub> c'<sub>4</sub>(0) – X. *J. Geophys. Res.* 106, 3685 – 3689.
- Stevens, M. H., Gustin, J., Ajello, J. M., Evans, J. S., Meier, R. R., Kochenash, A. J., Stephan, A. W., Stewart, A. I. F., Esposito, L. W., McClintock, W. E., Holsclaw, G., Bradley, E. T., Lewis, B. R., Heays, A. N., 2011. The production of Titan's ultraviolet nitrogen airglow. *J. Geophys. Res.* 116, A05304. doi: 10.1029/2010JA016284.
- Strickland, D. J., Bishop, J., Evans, J. S., Majeed, T., Shen, P. M., Cox, R. J., Link, R., Huffman, R. E., 1999. Atmospheric Ultraviolet Radiance Integrated Code (AURIC): Theory, software architecture, inputs, and selected results. *Journal of Quantitative Spectroscopy & Radiative Transfer* 62, 689 – 742. doi:10.1016/S0022-4073(98)00098-3.

- Strobel, D. F., Atreya, S. K., Bézard, B., Ferri, F., Flasar, F. M., Fulchignoni, M., Lellouch, E., Müller-Wodarg, I., 2009. Titan from cassini-huygens. Springer, Ch. Atmospheric Structure and Composition, pp. 235 – 257. doi:10.1007/978-1-4020-9215-2.
- Strobel, D. F., Shemansky, D. E., 1982. EUV emission from Titan's upper atmosphere: Voyager 1 encounter. *J. Geophys. Res.* 87, 1361. doi:10.1029/JA087iA03p01361.
- Tobiska, W. K., 2004. SOLAR2000 irradiances for climate change, aeronomy and space system engineering. *Adv. Space Res.* 34, 1736 – 1746. doi:10.1016/j.asr.2003.06.032.
- Woods, T. N., Eparvier, F. G., Bailey, S. M., Chamberlin, P. C., Lean, J., Rottman, G. J., Solomon, S. C., Tobiska, W. K., Woodraska, D. L., 2005. Solar EUV Experiment (SEE): Mission overview and first results. *J. Geophys. Res.* 110, A01312. doi: 10.1029/2004JA010765.



Table 1: Vertically-integrated overhead intensities of triplet transitions of N<sub>2</sub>.

Band	Intensity (R)				
	Min*			SEE	
	SEE	S2K	HEUVAC	Moderate <sup>§</sup>	Max. <sup>†</sup>
Vegard-Kaplan ( $A \rightarrow X$ ) (137–1155 nm)	132	163	121	257	371
130–150 nm	3.7E-2 <sup>‡</sup>	4.6E-2	3.4E-2	7.3E-2	1E-1
150–200 nm	6	7.5	5.5	12	16.7
200–300 nm	45.7	56	42.3	89.3	129
300–400 nm	51.2	63	47.3	100	144
400–800 nm	28.7	35	26.4	56	80.7
400–500 nm	20.9	25	19.2	40.9	58.9
500–800 nm	7.8	9.5	7.2	15.1	21.8
First Positive ( $B \rightarrow A$ ) (263–94129 nm)	114	141	106	223	322
600–800 nm	55.7	69	52	109	157
Second Positive ( $C \rightarrow B$ ) (268–1140 nm)	19	24	18	37	54.5
300–400 nm	17.5	22	16.6	34	50.3
Wu-Benesch ( $W \rightarrow B$ ) (399–154631 nm)	22	28	21	43.6	63.6
$B' \rightarrow B$ (312–37699 nm)	9.5	12	9	18.6	27.13
$E \rightarrow A$ (207–303 nm)	0.25	0.32	0.25	0.50	0.74
$E \rightarrow B$ (259–483 nm)	4E-2	5E-2	4E-2	8E-2	0.12
$E \rightarrow C$ (1113–10127 nm)	0.15	0.19	0.14	0.3	0.43
R1P <sup>¶</sup> ( $A \rightarrow B$ ) (739–74175 nm)	22	27	20	43	61.6

\*Solar minimum condition (F10.7=68).

§Solar moderate condition (F10.7=150).

†Solar maximum condition (F10.7=256).

‡3.7E-2 =  $3.7 \times 10^{-2}$ .

¶Reverse First Positive.

SEE=Solar EUV Experiment; S2K=SOLAR2000; HEUVAC solar EUV flux models

Table 2: Overhead intensities (in R) of N<sub>2</sub> Vegard-Kaplan ( $A^3\Sigma_u^+ \rightarrow X^1\Sigma_g^+$ ) band.

$\nu' \setminus \nu''$	0	1	2	3	4	5	6	7	8	9
0	1.4E-5 (2010)	1.9E-2 (2109)	2.5E-1 (2216)	1.2E+0 (2334)	3.2E+0 (2463)	5.6E+0 (2605)	7.1E+0 (2762)	6.8E+0 (2937)	5.0E+0 (3133)	2.9E+0 (3354)
1	3.1E-3 (1954)	1.1E-2 (2047)	2.8E-1 (2148)	1.1E+0 (2258)	1.5E+0 (2379)	7.9E-1 (2511)	1.7E-7 (2657)	1.2E+0 (2819)	4.1E+0 (2998)	6.0E+0 (3200)
2	3.2E-2 (1901)	3.0E-3 (1990)	9.1E-2 (2085)	2.8E-1 (2189)	7.4E-2 (2302)	2.0E-1 (2425)	1.3E+0 (2561)	1.7E+0 (2711)	5.3E-1 (2877)	1.2E-1 (3062)
3	1.1E-1 (1853)	6.2E-2 (1936)	2.5E-3 (2027)	1.3E-2 (2125)	6.4E-2 (2231)	4.8E-1 (2347)	4.4E-1 (2474)	8.7E-8 (2614)	7.1E-1 (2768)	1.5E+0 (2938)
4	2.5E-1 (1808)	1.6E-1 (1887)	6.7E-3 (1973)	1.9E-3 (2065)	9.0E-2 (2166)	1.3E-1 (2275)	4.1E-3 (2394)	4.1E-1 (2524)	5.4E-1 (2668)	2.4E-2 (2826)
5	4.3E-1 (1765)	2.3E-1 (1841)	5.7E-3 (1923)	1.8E-4 (2011)	2.4E-2 (2106)	5.2E-4 (2209)	1.3E-1 (2321)	2.2E-1 (2443)	1.3E-4 (2577)	3.6E-1 (2724)
6	6.9E-1 (1726)	2.4E-1 (1798)	9.4E-4 (1876)	7.8E-3 (1960)	5.6E-4 (2050)	1.7E-2 (2147)	9.5E-2 (2253)	4.3E-3 (2368)	1.8E-1 (2494)	2.6E-1 (2632)
7	1.1E+0 (1689)	1.9E-1 (1758)	4.2E-2 (1833)	3.2E-2 (1912)	2.5E-4 (1998)	1.5E-2 (2090)	1.5E-2 (2191)	4.8E-2 (2299)	1.7E-1 (2418)	1.1E-3 (2547)
8	1.0E+0 (1655)	6.2E-2 (1721)	1.1E-1 (1792)	2.7E-2 (1868)	1.2E-3 (1950)	8.0E-4 (2038)	8.5E-4 (2133)	5.0E-2 (2236)	1.4E-2 (2347)	7.8E-2 (2469)
9	5.9E-1 (1622)	2.7E-3 (1686)	9.6E-2 (1754)	4.7E-3 (1827)	7.2E-3 (1905)	3.1E-4 (1989)	1.9E-3 (2079)	8.4E-3 (2177)	4.2E-3 (2283)	4.5E-2 (2398)
10	2.6E-1 (1592)	3.2E-3 (1653)	5.0E-2 (1718)	1.4E-4 (1788)	7.6E-3 (1863)	6.4E-5 (1943)	1.1E-4 (2030)	1.1E-4 (2122)	5.7E-3 (2223)	4.5E-3 (2332)
11	1.2E-1 (1563)	9.3E-3 (1622)	2.0E-2 (1685)	2.7E-3 (1752)	4.1E-3 (1824)	1.7E-4 (1901)	7.8E-5 (1983)	7.4E-5 (2072)	1.5E-3 (2168)	3.8E-5 (2271)
12	5.6E-2 (1536)	1.2E-2 (1593)	7.3E-3 (1654)	4.4E-3 (1719)	1.4E-3 (1788)	7.2E-4 (1861)	1.2E-4 (1940)	1.5E-5 (2025)	1.2E-4 (2116)	5.4E-4 (2215)
13	2.7E-2 (1511)	1.0E-2 (1566)	1.8E-3 (1625)	4.0E-3 (1687)	1.7E-4 (1754)	8.9E-4 (1824)	1.8E-5 (1900)	1.2E-5 (1981)	3.1E-7 (2069)	2.9E-4 (2163)
14	1.3E-2 (1487)	7.9E-3 (1541)	2.1E-4 (1597)	2.8E-3 (1658)	1.6E-5 (1722)	6.6E-4 (1790)	1.4E-5 (1863)	4.6E-5 (1941)	2.7E-6 (2024)	5.3E-5 (2114)
15	6.7E-3 (1465)	5.7E-3 (1517)	8.5E-6 (1572)	1.7E-3 (1630)	2.0E-4 (1692)	3.4E-4 (1758)	8.7E-5 (1828)	3.5E-5 (1903)	7.1E-7 (1983)	1.8E-6 (2070)
16	3.4E-3 (1444)	3.9E-3 (1494)	1.7E-4 (1548)	8.3E-4 (1604)	3.4E-4 (1664)	1.1E-4 (1728)	1.3E-4 (1796)	8.2E-6 (1868)	9.5E-6 (1945)	3.8E-7 (2028)
17	1.8E-3 (1425)	2.6E-3 (1473)	3.3E-4 (1525)	3.4E-4 (1580)	3.6E-4 (1638)	1.5E-5 (1700)	1.3E-4 (1765)	2.2E-7 (1835)	1.5E-5 (1910)	4.7E-8 (1990)
18	9.5E-4 (1406)	1.7E-3 (1454)	4.0E-4 (1504)	1.1E-4 (1557)	3.0E-4 (1614)	1.3E-6 (1674)	9.0E-5 (1737)	9.3E-6 (1805)	1.1E-5 (1877)	8.0E-7 (1954)
19	5.1E-4 (1389)	1.1E-3 (1435)	4.0E-4 (1484)	2.0E-5 (1536)	2.1E-4 (1591)	1.9E-5 (1649)	4.6E-5 (1711)	2.0E-5 (1777)	4.3E-6 (1846)	3.1E-6 (1921)
20	2.8E-4 (1373)	6.9E-4 (1418)	3.6E-4 (1466)	5.0E-8 (1517)	1.4E-4 (1570)	3.8E-5 (1627)	1.8E-5 (1687)	2.5E-5 (1750)	4.1E-7 (1818)	4.5E-6 (1890)

Values in brackets show the band origin in Å.

Calculations are made using SEE solar flux (F10.7=68) on 23 June 2009 and at SZA = 60°.

Table 2: contd.

$\nu' \setminus \nu''$	10	11	12	13	14	15	16	17	18	19	20
0	1.4E+0 (3604)	5.3E-1 (3890)	1.6E-1 (4221)	4.1E-2 (4606)	8.5E-3 (5062)	1.4E-3 (5608)	1.9E-4 (6274)	2.0E-5 (7106)	1.6E-6 (8171)	1.0E-7 (9584)	4.8E-9 (11548)
1	5.7E+0 (3427)	3.8E+0 (3685)	1.9E+0 (3980)	7.5E-1 (4321)	2.3E-1 (4719)	5.6E-2 (5191)	1.1E-2 (5757)	1.7E-3 (6449)	2.0E-4 (7315)	1.8E-5 (8427)	1.3E-6 (9908)
2	1.9E+0 (3270)	4.0E+0 (3503)	4.3E+0 (3769)	3.1E+0 (4074)	1.6E+0 (4426)	5.9E-1 (4838)	1.7E-1 (5326)	3.9E-2 (5913)	6.8E-3 (6633)	9.2E-4 (7535)	9.4E-5 (8697)
3	7.4E-1 (3129)	3.9E-3 (3342)	1.1E+0 (3583)	2.6E+0 (3857)	2.9E+0 (4171)	2.0E+0 (4536)	9.7E-1 (4962)	3.5E-1 (5468)	9.2E-2 (6078)	1.8E-2 (6826)	2.8E-3 (7767)
4	4.5E-1 (3002)	1.2E+0 (3198)	5.9E-1 (3418)	2.0E-3 (3666)	7.7E-1 (3949)	1.8E+0 (4274)	1.9E+0 (4650)	1.2E+0 (5092)	5.3E-1 (5617)	1.7E-1 (6250)	3.9E-2 (7030)
5	5.1E-1 (2887)	2.0E-2 (3068)	3.9E-1 (3270)	9.2E-1 (3497)	3.7E-1 (3753)	2.0E-2 (4065)	7.0E-1 (4381)	1.3E+0 (4771)	1.2E+0 (5229)	6.8E-1 (5773)	2.6E-1 (6432)
6	3.9E-4 (2783)	4.0E-1 (2951)	4.4E-1 (3137)	1.0E-3 (3346)	4.6E-1 (3579)	7.5E-1 (3844)	1.8E-1 (4146)	8.7E-2 (4494)	7.4E-1 (4897)	1.1E+0 (5372)	8.2E-1 (5938)
7	2.7E-1 (2689)	2.6E-1 (2845)	2.0E-2 (3018)	5.1E-1 (3210)	3.3E-1 (3424)	2.2E-2 (3666)	6.0E-1 (3940)	6.1E-1 (4252)	4.6E-2 (4612)	2.3E-1 (5030)	8.3E-1 (5523)
8	1.4E-1 (2602)	5.2E-3 (2748)	2.6E-1 (2909)	1.2E-1 (3087)	7.2E-2 (3285)	3.9E-1 (3507)	1.1E-1 (3757)	9.3E-2 (4040)	4.6E-1 (4363)	2.5E-1 (4736)	1.2E-3 (5170)
9	1.3E-3 (2523)	7.0E-2 (2660)	5.1E-2 (2810)	2.4E-2 (2976)	1.4E-1 (3160)	1.6E-2 (3364)	8.7E-2 (3594)	1.6E-1 (3852)	6.8E-3 (4144)	1.0E-1 (4480)	1.9E-1 (4866)
10	8.2E-3 (2450)	2.1E-2 (2579)	1.3E-3 (2720)	4.0E-2 (2875)	7.0E-3 (3046)	2.8E-2 (3236)	4.6E-2 (3448)	2.3E-4 (3684)	5.6E-2 (3952)	3.8E-2 (4255)	2.9E-3 (4602)
11	5.8E-3 (2383)	5.5E-4 (2505)	8.7E-3 (2638)	5.6E-3 (2783)	5.3E-3 (2743)	1.6E-2 (3120)	1.6E-5 (3316)	2.0E-2 (3535)	8.9E-3 (3780)	5.6E-3 (4057)	2.5E-2 (4371)
12	1.2E-3 (2321)	7.7E-4 (2437)	3.6E-3 (2562)	1.8E-4 (2699)	6.3E-3 (2850)	4.1E-4 (3015)	6.4E-3 (3198)	4.3E-3 (3400)	2.3E-3 (3627)	9.8E-3 (3881)	3.7E-4 (4168)
13	2.6E-5 (2264)	1.0E-3 (2374)	2.6E-4 (2493)	1.5E-3 (2622)	1.1E-3 (2764)	1.2E-3 (2919)	2.7E-3 (3090)	2.7E-4 (3279)	4.1E-3 (3489)	2.6E-4 (3724)	3.3E-3 (3987)
14	4.2E-5 (2211)	3.5E-4 (2316)	6.1E-5 (2429)	8.2E-4 (2552)	1.4E-5 (2686)	1.3E-3 (2832)	4.3E-5 (2993)	1.5E-3 (3169)	4.9E-4 (3365)	1.1E-3 (3583)	1.5E-3 (3826)
15	5.5E-5 (2162)	4.0E-5 (2262)	1.9E-4 (2370)	1.3E-4 (2487)	3.0E-4 (2614)	3.1E-4 (2752)	2.9E-4 (2904)	6.0E-4 (3070)	1.4E-4 (3253)	9.4E-4 (3456)	2.2E-6 (3682)
16	2.0E-5 (2117)	4.0E-7 (2213)	1.1E-4 (2316)	5.3E-7 (2427)	2.3E-4 (2548)	2.2E-7 (2679)	3.5E-4 (2823)	1.3E-5 (2980)	4.2E-4 (3152)	8.0E-5 (3342)	3.8E-4 (3553)
17	2.5E-6 (2075)	8.0E-6 (2167)	2.8E-5 (2266)	3.1E-5 (2372)	6.5E-5 (2488)	5.6E-5 (2613)	1.1E-4 (2749)	6.5E-5 (2897)	1.7E-4 (3060)	4.8E-5 (3239)	2.5E-4 (3436)
18	2.1E-10 (2036)	6.2E-6 (2125)	1.9E-6 (2220)	3.3E-5 (2322)	3.3E-6 (2432)	6.8E-5 (2551)	4.8E-6 (2681)	1.0E-4 (2822)	9.4E-6 (2976)	1.3E-4 (3145)	2.2E-5 (3331)
19	1.3E-7 (2000)	1.8E-6 (2086)	3.6E-7 (2177)	1.5E-5 (2275)	2.8E-6 (2381)	3.2E-5 (2495)	7.7E-6 (2619)	4.8E-5 (2754)	1.2E-5 (2900)	9.4E-5 (3060)	1.2E-5 (3236)
20	4.0E-9 (1967)	1.5E-7 (2050)	1.3E-6 (2138)	3.6E-6 (2232)	7.8E-6 (2334)	6.4E-6 (2444)	1.9E-5 (2563)	7.5E-6 (2691)	3.0E-5 (2831)	8.6E-6 (2984)	4.0E-5 (3150)

Table 3: Overhead intensities (in R) of N<sub>2</sub> First Positive ( $B^3\Pi_g \rightarrow A^3\Sigma_u^+$ ) band.

$\nu' \setminus \nu''$	0	1	2	3	4	5	6	7	8	9
0	1.1E+1 (10469)	5.7E+0 (12317)	1.7E+0 (14895)	3.6E-1 (18739)	5.6E-2 (25084)	5.8E-3 (37523)	2.6E-4 (72916)	3.9E-8 (941292)	– –	– –
1	1.5E+1 (8883)	6.7E-2 (10179)	2.8E+0 (11878)	2.1E+0 (14201)	7.8E-1 (17569)	1.9E-1 (22882)	2.9E-2 (32502)	2.4E-3 (55202)	3.0E-5 (173933)	– –
2	6.9E+0 (7732)	9.0E+0 (8695)	1.7E+0 (9905)	3.4E-1 (11471)	1.3E+0 (13572)	8.4E-1 (16538)	3.0E-1 (21039)	6.8E-2 (28671)	9.2E-3 (44420)	4.1E-4 (95828)
3	1.4E+0 (6858)	9.3E+0 (7606)	2.4E+0 (8516)	2.9E+0 (9648)	7.6E-2 (11092)	3.6E-1 (12997)	5.6E-1 (15624)	3.1E-1 (19474)	1.0E-1 (25651)	2.0E-2 (37163)
4	1.4E-1 (6173)	2.8E+0 (6772)	7.1E+0 (7484)	1.3E-1 (8345)	2.1E+0 (9404)	5.3E-1 (10739)	1.3E-2 (12471)	2.3E-1 (14807)	2.2E-1 (18126)	1.0E-1 (23207)
5	6.4E-3 (5622)	3.5E-1 (6114)	3.2E+0 (6689)	3.8E+0 (7368)	1.4E-1 (8181)	8.9E-1 (9173)	6.7E-1 (10408)	4.5E-2 (11987)	4.1E-2 (14072)	1.1E-1 (16954)
6	1.3E-4 (5168)	2.0E-2 (5582)	5.0E-1 (6057)	2.6E+0 (6608)	1.5E+0 (7255)	4.7E-1 (8025)	2.0E-1 (8954)	4.6E-1 (10098)	1.3E-1 (11539)	2.1E-5 (13407)
7	1.0E-6 (4789)	4.8E-4 (5142)	3.4E-2 (5543)	5.3E-1 (6001)	1.7E+0 (6530)	4.0E-1 (7147)	4.9E-1 (7875)	9.0E-3 (8746)	2.2E-1 (9806)	1.3E-1 (11124)
8	1.0E-9 (4448)	3.9E-6 (4774)	9.2E-4 (5117)	4.1E-2 (5505)	4.4E-1 (5947)	9.6E-1 (6454)	5.5E-2 (7042)	3.3E-1 (7730)	1.1E-2 (8548)	6.7E-2 (9532)
9	3.0E-12 (4192)	4.0E-9 (4460)	8.5E-6 (4758)	1.3E-3 (5092)	4.3E-2 (5468)	3.3E-1 (5894)	4.8E-1 (6380)	5.3E-5 (6940)	1.7E-1 (7592)	3.6E-2 (8358)
10	1.3E-13 (3953)	3.5E-11 (4190)	8.0E-9 (4453)	1.3E-5 (4744)	1.5E-3 (5068)	3.7E-2 (5432)	2.2E-1 (5842)	2.0E-1 (6309)	1.1E-2 (6843)	6.7E-2 (7459)
11	7.4E-15 (3744)	5.6E-14 (3956)	7.8E-11 (4189)	1.1E-8 (4446)	1.5E-5 (4729)	1.4E-3 (5045)	2.7E-2 (5397)	1.2E-1 (5792)	7.2E-2 (6239)	1.8E-2 (6748)
12	8.4E-14 (3560)	7.7E-15 (3751)	8.0E-13 (3960)	1.3E-10 (4188)	1.1E-8 (4439)	1.4E-5 (4716)	1.1E-3 (5022)	1.7E-2 (5363)	5.8E-2 (5744)	1.9E-2 (6172)
13	2.1E-14 (3396)	3.0E-14 (3570)	1.0E-13 (3758)	3.3E-12 (3963)	2.0E-10 (4187)	9.2E-9 (4433)	1.1E-5 (4702)	7.3E-4 (5000)	9.6E-3 (5329)	2.6E-2 (5696)
14	4.4E-16 (3250)	4.2E-14 (3409)	9.2E-14 (3580)	7.2E-13 (3766)	8.5E-12 (3968)	2.8E-10 (4187)	7.7E-9 (4427)	9.2E-6 (4690)	5.3E-4 (4978)	5.8E-3 (5297)
15	5.5E-15 (3119)	6.1E-15 (3265)	6.9E-14 (3422)	3.7E-13 (3591)	1.7E-12 (3774)	1.6E-11 (3972)	3.6E-10 (4188)	6.7E-9 (4422)	8.2E-6 (4678)	4.2E-4 (4958)
16	1.2E-15 (3001)	1.4E-16 (3136)	3.0E-14 (3280)	1.4E-13 (3436)	6.7E-13 (3603)	3.1E-12 (3783)	2.9E-11 (3978)	4.2E-10 (4188)	5.5E-9 (4417)	6.9E-6 (4666)
17	2.4E-16 (2894)	6.2E-17 (3020)	5.1E-15 (3153)	2.9E-14 (3296)	1.8E-13 (3450)	9.8E-13 (3615)	4.0E-12 (3792)	3.3E-11 (3983)	3.4E-10 (4190)	3.3E-9 (4413)
18	8.0E-16 (2797)	3.0E-16 (2914)	2.1E-16 (3039)	4.0E-15 (3171)	3.9E-14 (3313)	2.3E-13 (3465)	9.6E-13 (3627)	3.9E-12 (3802)	3.1E-11 (3989)	2.3E-10 (4191)
19	3.9E-16 (3709)	5.6E-16 (2818)	2.5E-17 (2935)	4.7E-16 (3058)	9.4E-15 (3190)	5.5E-14 (3330)	3.0E-13 (3480)	1.2E-12 (3641)	4.8E-12 (3812)	3.8E-11 (3996)
20	5.7E-18 (2628)	7.3E-17 (2731)	4.4E-17 (2840)	1.3E-17 (2956)	1.0E-15 (3079)	7.5E-15 (3209)	5.2E-14 (3348)	2.5E-13 (3496)	9.6E-13 (3654)	4.2E-12 (3823)

Values in brackets show the band origin in Å.

Calculations are made using SEE solar flux on 23 June 2009 and at SZA = 60°.

Table 3: contd.

$\nu' \setminus \nu''$	10	11	12	13	14	15	16	17	18	19	20
3	2.0E-2 (66117)	1.9E-3 (274786)	– –	– –	– –	– –	– –	– –	– –	– –	– –
4	3.0E-2 (31941)	4.8E-3 (50449)	2.3E-4 (115737)	– –	– –	– –	– –	– –	– –	– –	– –
5	7.8E-2 (21186)	3.2E-2 (27999)	7.7E-3 (40761)	8.7E-4 (73199)	6.2E-6 (311787)	– –	– –	– –	– –	– –	– –
6	3.1E-2 (15923)	4.2E-2 (19487)	2.5E-2 (24916)	8.6E-3 (34172)	1.7E-3 (53448)	1.1E-4 (117886)	– –	– –	– –	– –	– –
7	1.5E-2 (12802)	2.9E-3 (15009)	1.5E-2 (18036)	1.5E-2 (22434)	7.4E-3 (29394)	2.3E-3 (42028)	3.5E-4 (71926)	7.7E-6 (229296)	– –	– –	– –
8	8.9E-2 (10737)	2.8E-2 (12248)	7.5E-4 (14192)	3.0E-3 (16781)	6.3E-3 (20392)	4.8E-3 (25765)	2.1E-3 (34576)	5.8E-4 (51601)	6.7E-5 (98056)	1.2E-7 (718231)	– –
9	1.1E-2 (9272)	4.4E-2 (10377)	2.6E-2 (11739)	4.8E-3 (13456)	2.3E-5 (15683)	1.7E-3 (18679)	2.4E-3 (22912)	1.6E-3 (29322)	6.5E-4 (40124)	1.6E-4 (62048)	1.4E-5 (129839)
10	3.8E-2 (8178)	4.6E-5 (9025)	1.5E-2 (10038)	1.7E-2 (11268)	6.4E-3 (12789)	6.3E-4 (14713)	1.4E-4 (17219)	7.7E-4 (20605)	8.4E-4 (25412)	5.2E-4 (32758)	2.1E-4 (45186)
11	1.9E-2 (7330)	2.5E-2 (8004)	1.8E-3 (8791)	3.1E-3 (9720)	7.6E-3 (10831)	4.9E-3 (12181)	1.3E-3 (13849)	5.4E-5 (15958)	1.1E-4 (18697)	3.0E-4 (22383)	2.9E-4 (27577)
12	1.5E-2 (6656)	1.8E-3 (7207)	1.2E-2 (7838)	3.1E-3 (8568)	1.5E-4 (9420)	2.3E-3 (10424)	2.5E-3 (11623)	1.2E-3 (13072)	2.4E-4 (14855)	1.4E-6 (17091)	5.0E-5 (19962)
13	4.2E-3 (6106)	8.6E-3 (6566)	1.1E-4 (7087)	4.3E-3 (7678)	2.5E-3 (8355)	8.3E-5 (9136)	4.3E-4 (10043)	9.5E-4 (11108)	7.2E-4 (12369)	2.8E-4 (13881)	4.6E-5 (15717)
14	1.2E-2 (5650)	6.4E-4 (6042)	4.7E-3 (6479)	9.9E-5 (6970)	1.4E-3 (7524)	1.6E-3 (8151)	3.1E-4 (8866)	2.5E-5 (9685)	2.9E-4 (10630)	3.6E-4 (11728)	2.2E-4 (13012)
15	3.9E-3 (5265)	6.2E-3 (5604)	1.8E-5 (5979)	2.5E-3 (6394)	3.5E-4 (6857)	3.6E-4 (7374)	9.0E-4 (7955)	3.9E-4 (8608)	1.5E-5 (9347)	5.8E-5 (10185)	1.5E-4 (11140)
16	3.2E-4 (4938)	2.5E-3 (5234)	3.0E-3 (5560)	4.9E-5 (5917)	1.2E-3 (6312)	4.4E-4 (6747)	4.4E-5 (7230)	4.1E-4 (7765)	3.2E-4 (8312)	6.9E-5 (9026)	9.3E-7 (9768)
17	4.4E-6 (4655)	1.8E-4 (4918)	1.2E-3 (5204)	1.1E-3 (5516)	1.1E-4 (5857)	3.6E-4 (6230)	2.9E-4 (6639)	7.5E-7 (7089)	1.1E-4 (7582)	1.6E-4 (8124)	7.1E-5 (8721)
18	1.9E-9 (4409)	2.6E-6 (4644)	9.8E-5 (4899)	5.5E-4 (5174)	3.4E-4 (5473)	1.0E-4 (5798)	8.6E-5 (6150)	1.5E-4 (6534)	1.4E-5 (6951)	2.0E-5 (7404)	6.0E-5 (7896)
19	2.1E-10 (4194)	1.5E-9 (4406)	2.2E-6 (4634)	7.4E-5 (4880)	3.5E-4 (5145)	1.4E-4 (5431)	1.0E-4 (5739)	2.0E-5 (6072)	8.9E-5 (6430)	2.6E-5 (6816)	1.5E-6 (7231)
20	3.3E-11 (4003)	1.4E-10 (4196)	9.7E-10 (4403)	1.4E-6 (4624)	4.3E-5 (4862)	1.7E-4 (5116)	4.2E-5 (5389)	6.3E-5 (5681)	1.3E-6 (5993)	3.6E-5 (6327)	2.1E-5 (6683)



Table 4: Overhead intensities (in R) of N<sub>2</sub> Second Positive ( $C^3\Pi_u \rightarrow B^3\Pi_g$ ) band.

$\nu' \setminus \nu''$	0	1	2	3	4	5	6	7	8	9
0	6.5E+0 (3370)	4.4E+0 (3576)	1.8E+0 (3804)	5.5E-1 (4058)	1.5E-1 (4343)	3.5E-2 (4665)	7.7E-3 (5032)	1.6E-3 (5452)	3.3E-4 (5938)	6.7E-5 (6507)
1	1.7E+0 (3158)	8.3E-2 (3338)	7.8E-1 (3536)	7.0E-1 (3754)	3.4E-1 (3997)	1.3E-1 (4268)	3.9E-2 (4573)	1.1E-2 (4317)	2.8E-3 (5309)	6.6E-4 (5759)
2	2.0E-1 (2976)	5.0E-1 (3135)	3.9E-2 (3309)	8.4E-2 (3499)	2.0E-1 (3709)	1.5E-1 (3942)	7.7E-2 (4200)	3.0E-2 (4489)	1.0E-2 (4813)	3.0E-3 (5180)
3	7.5E-3 (2818)	1.0E-1 (2961)	8.5E-2 (3115)	4.1E-2 (3284)	1.6E-3 (3468)	3.3E-2 (3671)	4.3E-2 (3894)	2.9E-2 (4140)	1.4E-2 (4415)	5.6E-3 (4722)
4	5.2E-5 (2684)	4.9E-3 (2812)	3.4E-2 (2952)	1.1E-2 (3102)	1.4E-2 (3266)	4.7E-4 (3445)	3.8E-3 (3641)	8.9E-3 (3856)	7.9E-3 (4093)	4.7E-3 (4355)

Values in brackets show the band origin in Å.

Calculations are made using SEE solar flux on 23 June 2009 and at SZA = 60°.

Table 4: contd.

$\nu' \setminus \nu''$	10	11	12	13	14	15	16	17	18	19	20
0	1.3E-5 (7181)	2.4E-6 (7992)	4.2E-7 (8985)	6.9E-8 (10228)	1.0E-8 (11828)	1.3E-9 (13962)	1.3E-10 (16944)	7.4E-12 (21403)	5.7E-16 (28779)	2.6E-13 (43302)	7.6E-14 (84991)
1	1.5E-4 (6281)	3.3E-5 (6893)	7.1E-6 (7619)	1.4E-6 (8495)	2.7E-7 (9571)	4.6E-14 (10921)	6.8E-09 (12665)	7.6E-10 (15000)	4.4E-11 (18285)	2.3E-14 (23236)	2.2E-12 (31536)
2	8.5E-4 (5599)	2.2E-4 (6080)	5.5E-5 (6638)	1.3E-5 (7293)	3.0E-6 (8071)	6.3E-7 (9011)	1.2E-7 (10166)	2.1E-8 (11618)	2.9E-9 (13495)	2.4E-10 (16014)	1.8E-12 (19563)
3	1.9E-3 (5067)	6.2E-4 (5458)	1.8E-4 (5904)	5.1E-5 (6416)	1.4E-5 (7011)	3.4E-6 (7709)	8.1E-7 (8539)	1.8E-7 (9541)	3.5E-8 (10771)	5.7E-9 (12317)	7.1E-10 (14315)
4	2.2E-3 (4648)	8.8E-4 (4974)	3.2E-4 (5342)	1.0E-4 (5758)	3.2E-5 (6233)	9.4E-6 (6778)	2.6E-6 (7412)	7.0E-7 (8155)	1.7E-7 (9037)	3.7E-8 (10101)	7.1E-9 (11406)

Values in brackets show the band origin in Å.

Calculations are made using SEE solar flux on 23 June 2009 and at SZA = 60°.

Table 5: Overhead intensities (in R) of N<sub>2</sub> Wu-Benesch ( $W^3\Delta_u \rightarrow B^3\Pi_g$ ) band.

$\nu' \setminus \nu''$	0	1	2	3	4	5	6	7	8	9
0	1.6E-1 (1361044)	— —	— —	— —	— —	— —	— —	— —	— —	— —
1	4.5E-1 (64311)	— —	— —	— —	— —	— —	— —	— —	— —	— —
2	6.5E-1 (33206)	7.3E-2 (76556)	— —	— —	— —	— —	— —	— —	— —	— —
3	5.6E-1 (22505)	4.9E-1 (36522)	9.0E-3 (94180)	— —	— —	— —	— —	— —	— —	— —
4	3.5E-1 (17092)	8.5E-1 (24124)	2.4E-1 (40502)	1.9E-4 (121693)	— —	— —	— —	— —	— —	— —
5	1.9E-1 (13825)	7.9E-1 (18090)	7.5E-1 (25962)	8.8E-2 (45362)	1.8E-4 (170594)	— —	— —	— —	— —	— —
6	8.0E-2 (11639)	5.2E-1 (14521)	9.8E-1 (19193)	4.9E-1 (28067)	1.8E-2 (51426)	1.6E-4 (281484)	— —	— —	— —	— —
7	3.0E-2 (10075)	2.7E-1 (12165)	7.9E-1 (15281)	8.6E-1 (20421)	2.3E-1 (30501)	8.7E-4 (59196)	1.1E-5 (774629)	— —	— —	— —
8	1.0E-2 (8900)	1.2E-1 (10493)	4.8E-1 (12732)	8.7E-1 (16112)	5.9E-1 (21794)	8.3E-2 (33343)	5.4E-4 (69497)	— —	— —	— —
9	3.3E-3 (7986)	4.5E-2 (9246)	2.4E-1 (10941)	6.2E-1 (13347)	7.5E-1 (17024)	3.3E-1 (23339)	1.9E-2 (36704)	1.5E-3 (83791)	— —	— —
10	9.8E-4 (7255)	1.6E-2 (8280)	1.0E-1 (9614)	3.5E-1 (11424)	6.2E-1 (14014)	5.3E-1 (18030)	1.5E-1 (25088)	1.6E-3 (40735)	1.2E-3 (104922)	— —
11	2.8E-4 (6658)	5.2E-3 (7511)	4.0E-2 (8592)	1.7E-1 (10009)	4.0E-1 (11943)	5.2E-1 (14742)	3.1E-1 (19145)	5.1E-2 (27084)	2.1E-4 (45654)	5.4E-4 (139282)
12	7.9E-5 (6160)	1.6E-3 (6883)	1.5E-2 (7781)	7.2E-2 (8925)	2.1E-1 (10432)	3.8E-1 (12505)	3.7E-1 (15536)	1.6E-1 (20386)	1.2E-2 (29381)	1.3E-3 (51783)
13	2.2E-5 (5740)	4.9E-4 (6363)	4.9E-3 (7122)	2.8E-2 (8069)	1.0E-1 (9281)	2.3E-1 (10886)	3.1E-1 (13114)	2.3E-1 (16408)	6.7E-2 (21774)	1.4E-3 (32050)
14	6.2E-6 (5380)	1.5E-4 (5924)	1.7E-3 (6577)	1.1E-2 (7376)	4.6E-2 (8375)	1.3E-1 (9661)	2.3E-1 (11376)	2.4E-1 (13776)	1.4E-1 (17369)	2.5E-2 (23337)
15	1.5E-6 (5069)	4.1E-5 (5549)	5.0E-4 (6118)	3.6E-3 (6803)	1.7E-2 (7645)	5.5E-2 (8702)	1.2E-1 (10070)	1.7E-1 (11905)	1.4E-1 (14497)	6.1E-2 (18431)
16	3.8E-7 (4798)	1.1E-5 (5225)	1.5E-4 (5727)	1.2E-3 (6323)	6.4E-3 (7044)	2.3E-2 (7932)	6.0E-2 (9052)	1.1E-1 (10509)	1.2E-1 (12478)	8.3E-2 (15286)
17	9.2E-8 (4559)	3.1E-6 (4943)	4.5E-5 (5390)	3.9E-4 (5915)	2.3E-3 (6541)	9.4E-3 (7300)	2.8E-2 (8238)	5.9E-2 (9427)	8.6E-2 (10982)	8.1E-2 (13100)
18	2.0E-8 (4347)	7.8E-7 (4695)	1.3E-5 (5096)	1.2E-4 (5564)	7.9E-4 (6114)	3.6E-3 (6772)	1.2E-2 (7572)	2.9E-2 (8565)	5.1E-2 (9830)	6.3E-2 (11493)
19	3.9E-9 (4159)	1.8E-7 (4476)	3.4E-6 (4839)	3.7E-5 (5259)	2.6E-4 (5748)	1.3E-3 (6325)	4.9E-3 (7018)	1.3E-2 (7863)	2.8E-2 (8916)	4.1E-2 (10263)
20	5.5E-10 (3990)	3.8E-8 (4281)	8.7E-7 (4612)	1.1E-5 (4991)	8.3E-5 (5430)	4.6E-4 (5943)	1.9E-3 (6550)	5.8E-3 (7280)	1.4E-2 (8174)	2.4E-2 (9292)

Values in brackets show the band origin in Å.

Calculations are made using SEE solar flux on 23 June 2009 and at SZA = 60°.

Table 5: contd.

$\nu' \setminus \nu''$	10	11	12	13	14	15	16	17
12	1.4E-4 (204814)	— —	— —	— —	— —	— —	— —	— —
13	1.5E-3 (59621)	1.5E-5 (378656)	— —	— —	— —	— —	— —	— —
14	1.7E-5 (35186)	1.1E-3 (69984)	4.9E-8 (2189094)	— —	— —	— —	— —	— —
15	6.0E-3 (25109)	5.4E-4 (38919)	5.2E-4 (84300)	— —	— —	— —	— —	— —
16	2.5E-2 (19612)	8.6E-4 (27132)	7.9E-4 (43431)	2.0E-4 (105325)	— —	— —	— —	— —
17	4.3E-2 (16153)	8.8E-3 (20931)	2.4E-6 (29461)	6.6E-4 (48989)	5.5E-5 (139141)	— —	— —	— —
18	4.9E-2 (13778)	2.0E-2 (17109)	2.4E-3 (22413)	1.4E-4 (32169)	4.1E-4 (55990)	1.0E-5 (202357)	— —	— —
19	4.2E-2 (12047)	2.7E-2 (14519)	8.3E-3 (18167)	4.0E-4 (24089)	2.8E-4 (35352)	2.1E-4 (65067)	9.5E-7 (362190)	— —
20	3.0E-2 (10731)	2.6E-2 (12649)	1.3E-2 (15332)	2.9E-3 (19345)	9.9E-6 (25997)	2.7E-4 (39142)	8.6E-5 (77278)	5.7E-9 (1546312)

Table 6: Overhead intensities (in R) of  $N_2$   $B'^3\Sigma_u^- \rightarrow B^3\Pi_g$  band.

$\nu' \setminus \nu''$	0	1	2	3	4	5	6	7	8	9
0	1.2E-2 (15280)	3.4E-3 (20664)	2.5E-4 (31616)	3.4E-6 (65977)	– –	– –	– –	– –	– –	– –
1	6.2E-2 (12442)	2.9E-3 (15793)	1.1E-2 (21479)	1.7E-3 (33241)	3.1E-5 (71941)	– –	– –	– –	– –	– –
2	1.0E-1 (10520)	8.6E-2 (12820)	3.2E-3 (16329)	1.3E-2 (22337)	4.1E-3 (34981)	1.0E-4 (78778)	– –	– –	– –	– –
3	9.4E-2 (9132)	2.2E-1 (10816)	4.7E-2 (13212)	2.5E-2 (16887)	7.5E-3 (23237)	6.1E-3 (36843)	1.9E-4 (86653)	– –	– –	– –
4	5.9E-2 (8083)	2.6E-1 (9375)	2.4E-1 (11123)	5.9E-3 (13618)	4.8E-2 (17468)	1.7E-3 (24181)	6.4E-3 (38831)	2.4E-4 (95765)	– –	– –
5	2.9E-2 (7262)	2.0E-1 (8289)	3.8E-1 (9626)	1.6E-1 (11440)	4.0E-3 (14040)	5.2E-2 (18072)	3.0E-5 (25169)	5.3E-3 (40949)	2.5E-4 (106355)	– –
6	1.2E-2 (6603)	1.1E-1 (7441)	3.3E-1 (8501)	3.6E-1 (9886)	6.4E-2 (11769)	2.8E-2 (14476)	3.9E-2 (18699)	1.8E-3 (26201)	3.6E-3 (43199)	2.1E-4 (118707)
7	4.3E-3 (6062)	5.0E-2 (6761)	2.2E-1 (7625)	4.0E-1 (8721)	2.6E-1 (10154)	1.0E-2 (12107)	4.8E-2 (14927)	2.2E-2 (19349)	4.4E-3 (27275)	2.0E-3 (45581)
8	1.4E-3 (5610)	2.0E-2 (6204)	1.1E-1 (6924)	2.9E-1 (7815)	3.6E-1 (8947)	1.4E-1 (10430)	5.4E-4 (12457)	5.2E-2 (15392)	8.8E-3 (20021)	5.7E-3 (28389)
9	4.2E-4 (5227)	7.0E-3 (5739)	4.8E-2 (6350)	1.7E-1 (7092)	3.1E-1 (8011)	2.6E-1 (9180)	5.1E-2 (10714)	1.1E-2 (12817)	4.3E-2 (15872)	2.2E-3 (20712)
10	1.2E-4 (4890)	2.3E-3 (5345)	1.8E-2 (5872)	8.1E-2 (4500)	2.0E-1 (7264)	2.7E-1 (8213)	1.6E-1 (9419)	1.1E-2 (11007)	2.3E-2 (13187)	2.8E-2 (16364)
11	3.4E-5 (4614)	7.1E-4 (5008)	6.6E-3 (5467)	3.4E-2 (6008)	1.1E-1 (6655)	2.0E-1 (7442)	2.0E-1 (8420)	7.6E-2 (9666)	1.3E-4 (11308)	2.6E-2 (13566)
12	9.2E-6 (4365)	2.1E-4 (4716)	2.2E-3 (5121)	1.3E-2 (5592)	4.9E-2 (6149)	1.2E-1 (6815)	1.7E-1 (7625)	1.3E-1 (8633)	2.9E-2 (9919)	2.4E-3 (11616)
13	2.5E-6 (4145)	6.2E-5 (4460)	7.0E-4 (4821)	4.7E-3 (5236)	2.0E-2 (5721)	5.8E-2 (6294)	1.1E-1 (6979)	1.2E-1 (7817)	6.9E-2 (8853)	7.2E-3 (10179)
14	6.5E-7 (3950)	1.8E-5 (4235)	2.2E-4 (4559)	1.6E-3 (4929)	7.9E-3 (5356)	2.6E-2 (5854)	6.0E-2 (6443)	9.1E-2 (7148)	8.2E-2 (8007)	3.2E-2 (9078)
15	1.7E-7 (3775)	4.9E-6 (4035)	6.5E-5 (4328)	5.3E-4 (4660)	2.9E-3 (5040)	1.1E-2 (5479)	3.0E-2 (5991)	5.5E-2 (6596)	6.8E-2 (7322)	4.8E-2 (8206)
16	4.4E-8 (3619)	1.4E-6 (3857)	1.9E-5 (4123)	1.7E-4 (4424)	1.0E-3 (4765)	4.3E-3 (5155)	1.3E-2 (5606)	2.9E-2 (6132)	4.5E-2 (6754)	4.6E-2 (7500)
17	1.1E-8 (3477)	3.7E-7 (3696)	5.6E-6 (3940)	5.2E-5 (4214)	3.4E-4 (4522)	1.6E-3 (4872)	5.4E-3 (5273)	1.4E-2 (5737)	2.6E-2 (6277)	3.4E-2 (6917)
18	2.8E-9 (3349)	9.9E-8 (3552)	1.6E-6 (3776)	1.6E-5 (4027)	1.1E-4 (4308)	5.6E-4 (4624)	2.1E-3 (4984)	6.2E-3 (5395)	1.3E-2 (5871)	2.1E-2 (6427)
19	6.6E-10 (3232)	2.6E-8 (3420)	4.5E-7 (3629)	4.8E-6 (3859)	3.6E-5 (4116)	2.0E-4 (4404)	8.1E-4 (4729)	2.6E-3 (5099)	6.3E-3 (5521)	1.2E-2 (6010)
20	1.4E-10 (3125)	6.4E-9 (3301)	1.2E-7 (3495)	1.4E-6 (3708)	1.1E-5 (3945)	6.6E-5 (4209)	3.0E-4 (4504)	1.0E-3 (4838)	2.8E-3 (5217)	5.9E-3 (5651)

Values in brackets show the band origin in Å.

Calculations are made using SEE solar flux on 23 June 2009 and at  $SZA = 60^\circ$ .

Table 6: contd.

$\nu' \setminus \nu''$	10	11	12	13	14	15	16	17	18	19	20
7	1.5E-4 (133152)	– –	– –	– –	– –	– –	– –	– –	– –	– –	– –
8	9.6E-4 (48087)	9.9E-5 (150065)	– –	– –	– –	– –	– –	– –	– –	– –	– –
9	5.7E-3 (29540)	3.8E-4 (50709)	5.9E-5 (169831)	– –	– –	– –	– –	– –	– –	– –	– –
10	1.1E-4 (21422)	4.6E-3 (30723)	1.2E-4 (53427)	3.2E-5 (192800)	– –	– –	– –	– –	– –	– –	– –
11	1.6E-2 (16868)	1.9E-4 (22148)	3.3E-3 (31929)	2.5E-5 (56215)	1.7E-5 (219162)	– –	– –	– –	– –	– –	– –
12	2.3E-2 (13955)	7.3E-3 (17383)	7.6E-4 (22886)	2.1E-3 (33152)	1.4E-6 (59037)	8.5E-6 (248754)	– –	– –	– –	– –	– –
13	6.6E-3 (11932)	1.7E-2 (14352)	2.8E-3 (17907)	1.1E-3 (23633)	1.3E-3 (34378)	9.9E-7 (61844)	4.2E-6 (280746)	– –	– –	– –	– –
14	6.0E-4 (10446)	8.5E-3 (12255)	1.0E-2 (14756)	7.9E-4 (18437)	1.1E-3 (24383)	7.2E-4 (35595)	4.4E-6 (64575)	2.1E-6 (313255)	– –	– –	– –
15	1.3E-2 (9308)	2.2E-4 (10718)	8.1E-3 (12584)	5.9E-3 (15166)	1.2E-4 (18972)	9.8E-4 (25131)	3.9E-4 (36786)	6.2E-6 (67157)	1.1E-6 (343066)	– –	– –
16	2.5E-2 (8410)	3.6E-3 (9545)	1.3E-3 (10996)	6.3E-3 (12918)	3.0E-3 (15581)	1.2E-0 (19507)	7.5E-4 (25869)	2.0E-4 (37932)	6.2E-6 (69506)	6.4E-7 (365813)	– –
17	2.8E-2 (7683)	1.2E-2 (8619)	5.6E-4 (9786)	2.1E-3 (11280)	4.4E-3 (13258)	1.3E-3 (15997)	4.0E-5 (20039)	5.2E-4 (26589)	1.0E-4 (39011)	5.1E-6 (71531)	4.0E-7 (376997)
18	2.4E-2 (7084)	1.6E-2 (7872)	4.7E-3 (8834)	1.3E-9 (10033)	2.2E-3 (11568)	2.7E-3 (13600)	5.3E-4 (16414)	8.8E-5 (20564)	3.4E-4 (27283)	5.0E-5 (40001)	3.8E-6 (73141)
19	1.6E-2 (6581)	1.5E-2 (7255)	8.2E-3 (8065)	1.5E-3 (9052)	1.9E-4 (10284)	1.9E-3 (11859)	1.6E-3 (13944)	1.8E-4 (16829)	1.1E-4 (21077)	2.2E-4 (27939)	2.4E-5 (40875)
20	9.6E-3 (6153)	1.1E-2 (6739)	8.9E-3 (7432)	3.8E-3 (8262)	3.2E-4 (9276)	4.2E-4 (10539)	1.4E-3 (12154)	8.4E-4 (14289)	4.7E-5 (17238)	1.0E-4 (21572)	1.3E-4 (28548)

Values in brackets show the band origin in Å.

Calculations are made using SEE solar flux on 23 June 2009 and at SZA = 60°.



Table 7: Overhead intensities (in R) of  $E^3\Sigma_g^+ \rightarrow A^3\Sigma_u^+$ ,  $E^3\Sigma_g^+ \rightarrow B^3\Pi_g$ , and  $E^3\Sigma_g^+ \rightarrow C^3\Pi_u$  bands of  $N_2$ .

$\nu' \setminus \nu''$	0	1	2	3	4	5	6	7	8	9	10
$E^3\Sigma_g^+ \rightarrow A^3\Sigma_u^+$											
0	8.9E-3 (2173)	2.8E-2 (2243)	4.5E-2 (2316)	5.0E-2 (2392)	4.1E-2 (2472)	2.8E-2 (2555)	1.6E-2 (2643)	7.7E-3 (2734)	3.3E-3 (2830)	1.2E-3 (2930)	3.9E-4 (3035)
1	2.7E-3 (2074)	6.2E-3 (2138)	7.0E-3 (2204)	4.8E-3 (2273)	2.2E-3 (2345)	5.6E-4 (2420)	3.9E-5 (2498)	2.0E-5 (2580)	8.6E-5 (2665)	1.0E-4 (2754)	7.8E-5 (2846)
$E^3\Sigma_g^+ \rightarrow B^3\Pi_g$											
0	7.5E-3 (2742)	1.1E-2 (2877)	9.2E-3 (3022)	5.7E-3 (3181)	2.9E-3 (3353)	1.3E-3 (3542)	5.6E-4 (3749)	2.2E-4 (3978)	8.3E-5 (4230)	3.0E-5 (4511)	1.0E-5 (4826)
1	5.6E-4 (2587)	2.0E-4 (2707)	1.0E-6 (2835)	5.8E-5 (2974)	1.2E-4 (3124)	1.2E-4 (3288)	8.0E-5 (3465)	4.6E-5 (3660)	2.3E-5 (3872)	1.1E-5 (4107)	4.6E-6 (4365)
$E^3\Sigma_g^+ \rightarrow C^3\Pi_u$											
0	1.3E-1 (14713)	1.1E-2 (20824)	4.1E-4 (34947)	2.6E-6 (101275)	— —	— —	— —	— —	— —	— —	— —
1	2.3E-3 (11134)	2.3E-3 (14312)	5.5E-4 (19816)	3.9E-5 (31522)	7.4E-7 (71884)	— —	— —	— —	— —	— —	— —

Values in brackets show the band origin in Å.

Calculations are made using SEE solar flux on 23 June 2009 and at SZA = 60°.

Table 8: Overhead intensities (in R) of N<sub>2</sub> Reverse First Positive ( $A^3\Sigma_u^+ \rightarrow B^3\Pi_g$ ) band.

$\nu' \setminus \nu''$	0	1	2	3	4	5	6	7	8
8	1.5E+0 (88467)	— —	— —	— —	— —	— —	— —	— —	— —
9	1.9E+0 (42771)	7.0E-1 (158042)	— —	— —	— —	— —	— —	— —	— —
10	8.2E-1 (28438)	2.3E+0 (55215)	8.5E-3 (741757)	— —	— —	— —	— —	— —	— —
11	2.5E-1 (21436)	1.5E+0 (33788)	1.2E+0 (77920)	— —	— —	— —	— —	— —	— —
12	7.7E-2 (17292)	6.9E-1 (24523)	1.6E+0 (41640)	3.1E-1 (132578)	— —	— —	— —	— —	— —
13	2.2E-2 (14555)	2.5E-1 (19361)	9.5E-1 (28664)	9.9E-1 (54305)	7.9E-3 (448147)	— —	— —	— —	— —
14	6.3E-3 (12617)	8.7E-2 (16076)	4.5E-1 (22007)	9.0E-1 (34521)	3.9E-1 (78216)	— —	— —	— —	— —
15	1.9E-3 (11175)	3.0E-2 (13806)	1.9E-1 (17964)	5.5E-1 (25513)	6.3E-1 (43455)	7.1E-2 (140462)	— —	— —	— —
16	5.7E-4 (10063)	9.9E-3 (12148)	7.3E-2 (15254)	2.8E-1 (20373)	5.1E-1 (30393)	3.0E-1 (58790)	5.0E-4 (710500)	— —	— —
17	1.8E-4 (9181)	3.4E-3 (10886)	2.8E-2 (13316)	1.3E-1 (17057)	3.1E-1 (23560)	3.6E-1 (37662)	8.3E-2 (91328)	— —	— —
18	5.8E-5 (8468)	1.2E-3 (9897)	1.1E-2 (11865)	5.5E-2 (14747)	1.7E-1 (19370)	2.8E-1 (27985)	1.9E-1 (49675)	6.8E-3 (207470)	— —
19	1.9E-5 (7880)	4.1E-4 (9103)	4.0E-3 (10763)	2.3E-2 (13052)	8.3E-2 (16548)	1.8E-1 (22452)	2.0E-1 (34558)	6.1E-2 (73390)	— —
20	6.5E-6 (7390)	1.5E-4 (8456)	1.5E-3 (9852)	9.8E-3 (11761)	4.0E-2 (14525)	1.0E-1 (18884)	1.6E-1 (26773)	1.0E-1 (45371)	8.3E-3 (142399)

Values in brackets show the band origin in Å.

Calculations are made using SEE solar flux on 23 June 2009 and at SZA = 60°.